Catalysis Science & Technology

ROYAL SOCIETY OF CHEMISTRY

PAPER

View Article Online
View Journal | View Issue

Check for updates

Cite this: *Catal. Sci. Technol.*, 2025, 15, 563

Structural contributions of Zn in enhancing CO_2 hydrogenation to methanol over Zn_xZrO_y catalysts†

Zinat Zanganeh, Max Bols, Parviz Yazdani, Hilde Poelman and Mark Saeys *

Single-reactor CO_2 conversion to light olefins *via* methanol is currently obstructed by the incompatible reaction conditions for the CO_2 to methanol and methanol to olefin steps. The conventional Cu/ZnO–Al_2O_3 CO_2 hydrogenation catalysts produce excessive CO and rapidly deactivate at the high temperatures preferred for methanol to olefins with zeolite or SAPO catalysts. Zn_xZrO_y catalysts are a promising alternative to Cu/ZnO–Al_2O_3. We studied Zn_xZrO_y with varying Zn doping levels, using XRD, XPS, H_2-TPR, CO_2-TPD, N_2-physisorption, DRIFT, and Raman spectroscopy, along with CO_2 conversion and methanol selectivity measurements, to examine structure-performance relationships in CO_2 hydrogenation to methanol. The interplay between dopant concentration, calcination temperature, and crystal structure dictates the catalyst's phase composition, which correlates with catalytic performance. The pristine ZrO_2 is a mixture of tetragonal and monoclinic phases. At Zn/Zr = 0.01, the tetragonal phase is dominant, while for Zn/Zr = 0.07–0.28, the cubic phase is obtained. Above Zn/Zr = 0.28, phase separation of ZnO occurs. For CO_2 hydrogenation to methanol, a Zn/Zr = 0.07–0.28 performs best. Zinc addition increases catalyst surface area, pore volume, basicity, and reducibility. XPS analysis reveals zinc enrichment near the surface and the formation of Zr–O–Zn species upon Zn incorporation into ZrO_2. A clear correlation between Zn content and catalyst activity is generally absent, but this relationship becomes evident in cubic-phase materials. At least in part, the relevance of zinc doping for CO_2 to methanol lies in its ability to distort the structure of zirconia, creating a cubic phase, with implications for selectivity that correlate with the adsorption of CO_2 and H_2.

Received 2nd October 2024,
Accepted 9th December 2024

DOI: 10.1039/d4cy01175a

rsc.li/catalysis

Open Access Article. Published on 12 December 2024. Downloaded on 2/17/2026 1:18:50 AM.
This article is licensed under a Creative Commons Attribution 3.0 Unported Licence.

1. Introduction

Catalytic hydrogenation of CO_2 to methanol (CTM) is an exothermic reaction facing slow reaction kinetics at low temperatures and low, thermodynamically limited selectivity at higher temperatures. The predominant methanol production route converts methane-derived syngas to methanol at 200–300 °C over a benchmark Cu/ZnO–Al_2O_3 catalyst through a CO_2 intermediate, involving water–gas-shift, with additional CO_2 feeding to match the net reaction stoichiometry.[1] To circumvent the thermodynamic limitation and enable higher temperature conditions, a tandem process is considered with *in situ* methanol to olefins (MTO) conversion over a Brønsted acid catalyst, regularly a zeolite or SAPO material.[2,3] The CTM-MTO tandem offers a direct selective route to C_2–C_3 olefins[4] as an alternative to Fischer–Tropsch synthesis with limited selectivity to light olefins.[5] The MTO reaction is optimized above 380 °C. This is a mismatch with the lower temperatures required for existing CTM catalysts, which are selective to CO instead of methanol at these high temperatures.[6] Several alternative CTM catalysts are considered. Zinc-doped zirconium oxide (Zn_xZrO_y) is particularly interesting for its improved CO_2 to methanol conversions and selectivity at higher temperatures, achieving 85% methanol selectivity at 320 °C.[7] Other metal dopants in zirconia have also been explored, yielding promising catalysts with diverging specifications.[6,8–10]

Most studies attribute zinc's promotional effect to its incorporation in the active sites interacting with CO_2 and H_2.[7,11] H_2-TPR measurements demonstrate that Zn addition enhances reducibility, increasing H_2 consumption and shifting it to lower temperatures.[12] A lowered take-off temperature for H_2–D_2 isotope scrambling, from 250 to 147 °C, is reported in Zn-doped *versus* undoped ZrO_2.[13] DFT calculations support this finding, indicating a low-barrier heterolytic H_2 dissociation on Zn_xZrO_y with the formation of Zn–H.[13] Zn addition may affect both surface oxygen

Laboratory for Chemical Technology, Ghent University, Technologiepark 125, B-9052 Ghent, Belgium. E-mail: mark.saeys@ugent.be

† Electronic supplementary information (ESI) available. See DOI: https://doi.org/10.1039/d4cy01175a

Open Access Article. Published on 12 December 2024. Downloaded on 2/17/2026 1:18:50 AM. This article is licensed under a Creative Commons Attribution 3.0 Unported Licence.

concentration and its chemical nature. Counteracting the beneficial effect of surface oxygen in H_2 activation for CTM conversion,[14] oxygen vacancies have been reported as active sites for CO_2 activation in this process. Through EPR and XPS measurements, several types of oxygen vacancies and their concentrations have been associated with coordinatively unsaturated Zr atoms (CUS-Zr). These surface species were correlated to CO_2 adsorption and reverse water gas shift (RWGS) activity.[15] However, various forms of CO_2 adsorption on the ZrO_2 surface are described.[16–20] Among these, the insertion of CO_2 into Zr–OH is associated with oxygen vacancies and CUS-Zr on the surface.[17,21,22] Besides CO_2 and H_2 activation, combining activated CO_2 and H_2 on the surface to form intermediates towards methanol is required. DFT has suggested that Zn facilitates the hydrogenation of surface Zr-bound intermediates through the proximity of Zn–H surface species.[13] Differences in surface intermediates and weaker CO_2 adsorption have been observed in DRIFTS on Zn_xZrO_y compared to ZrO_2.[13,23] It has been suggested that formate's C–O bond cleavage is easier on asymmetric Zn–O–Zr sites than on symmetric Zr–O–Zr sites, facilitating the formation of C–H bonds and methanol synthesis.[13,24]

Numerous additional explanations for the Zn promotional effect are found in literature, which are not necessarily mutually exclusive. XRD results show that Zn addition contracts the ZrO_2 crystal lattice, forms a solid solution, and alters ZrO_2 crystal phases.[12,23,25] The incorporation of ZnO nanoparticles into the ZrO_2 matrix is pointed out by EXAFS and correlates with the formation of Zn–O–Zr species.[11] Some researchers point at the ZnO–ZrO_2 interface as the dominant active site in CO_2 hydrogenation.[11,23,26] Other researchers, however, hypothesize that the growth of ZnO_x clusters during the reaction improves methanol synthesis by enhancing H_2 dissociation.[27] ZrO_2 inherently contains weak Zr^{4+}–O^{2-} Lewis acid–base (LAB) pairs,[28] whose reactivity in heterolytic H_2 dissociation is influenced by the crystal phase, exposed facets, and the orientation of LAB pair sites.[29,30] The introduction of Zn distorts the ZrO_2 lattice, leading to changes in both bulk and surface properties.

Zn can influence the concentration, nature, and proximity of Zr–OH, surface oxygen, and CUS-Zr in various ways while also introducing Zn–H, Zn–O–Zr, Zn–O–Zn, and ZnO_x motifs. Conclusive evidence for their relative contributions to CTM activity and selectivity is lacking. To offer another viewpoint to this puzzle, this study investigates the association between Zn doping and the ZrO_2 crystal phase and its subsequent impact on CTM. The aspect of the crystal phase has been largely overlooked in the Zn promotional effect, in contrast to other promotor metals (Y, Mg, Ca,…).[31,32] Most studies report ZrO_2 transitioning to the tetragonal phase after Zn addition.[11,13,22,26,33,34] Notably, a recent study emphasized the influence of the ZrO_2 crystal phase on methanol synthesis, showing that the tetragonal phase achieved higher methanol selectivity and space–time yield compared to the monoclinic phase. This was attributed to well-dispersed ZnO clusters on tetragonal ZrO_2, particularly under catalytic conditions.[26] However, doping ZrO_2 with Zn has been reported by several authors to induce a crystal structure alteration, stabilizing the cubic phase either in the bulk *via* coprecipitation or near the surface through impregnation.[7,23] Despite these observations, the direct relationship between the cubic phase of doped ZrO_2 and CTM catalysis has so far not been investigated.[35–37]

We prepared Zn_xZrO_y through coprecipitation, with Zn/Zr molar ratios ranging from 0.01 to 0.56. $Zn_{0.19}ZrO_y$ samples are calcined at various temperatures. We measure surface area, pore volume, temperature-programmed reducibility, CO_2 uptake, XRD, Raman, DRIFT and XPS spectra, and CTM catalysis to correlate structure and performance. The data indicate that the 'one fits all' active-site or surface structure explanations suggested in the literature are likely incomplete descriptions of the Zn promotion of ZrO_x for CTM.

2. Experimental

2.1. Catalyst synthesis

Zn_xZrO_y samples were synthesized through coprecipitation, using nitrate precursors of zinc and zirconium, and sodium carbonate as the precipitating agent. Zinc nitrate hexahydrate ($Zn(NO_3)_2{\cdot}6H_2O$, Sigma-Aldrich, purity ≥ 99%) was dissolved in a variable ratio into a 0.11 M solution of zirconium oxynitrate ($ZrO(NO_3)_2{\cdot}5H_2O$, Sigma-Aldrich, purity ≥ 98%) under stirring at 65 °C. Subsequently, a 0.30 M sodium carbonate solution (Na_2CO_3, Sigma-Aldrich, purity ≥ 99%) was added dropwise as the precipitating agent until the pH reached 9. The resulting suspension was aged for one hour at 65 °C. The precipitate was washed with deionized water until a pH of 7 was obtained. After filtration, the obtained material was dried overnight at 80 °C and then calcined for 3 hours at 500 °C under static air (heating ramp of 3 °C min^{-1}). The dried $Zn_{0.19}ZrO_y$ was also calcined at 550, 700, and 800 °C using the same heating ramp. The catalysts are denoted as Zn_xZrO_y-*T*, where *x* indicates the Zn/Zr molar ratio and *T* is the calcination temperature. The ZnO reference sample was synthesized using the same procedure by precipitating zinc nitrate hexahydrate with sodium carbonate, followed by aging, filtration, washing, and drying, but it was calcined at 350 °C.

2.2. Catalyst characterization

X-ray diffraction (XRD) measurements of the calcined catalysts were conducted on a Siemens Diffractometer Kristalloflex D5000, applying Cu Kα radiation (λ = 0.154 nm). The powder diffraction pattern was recorded in a 2θ range of 20–70° with a step size of 0.025°. The data were analysed employing DIFFRAC. EVA V5.2 software. Raman spectra of the powdered samples were recorded on a Raman spectrograph using a KAISER optical system coupled with a 532 nm laser source. The textural properties of the as-prepared catalysts were analysed by nitrogen adsorption/desorption isotherms at −196 °C in a Micrometrics Tristar-II 3020 instrument. Before the measurements, 400 mg of the calcined samples (150–250 μm) were degassed at 350 °C for 6 hours using a Micromeritics Smart Prep device. The data were

 This journal is © The Royal Society of Chemistry 2025

Open Access Article. Published on 12 December 2024. Downloaded on 2/17/2026 1:18:50 AM. This article is licensed under a Creative Commons Attribution 3.0 Unported Licence.

analysed using MicroActive software version 5.00. The specific surface area was determined using the Brunauer–Emmett–Teller (BET) method, utilizing nitrogen adsorption data at relative pressures between 0.05 and 0.30 to estimate surface area based on multilayer adsorption theory. The pore volume and pore size were calculated using the Barrett–Joyner–Halenda (BJH) method, derived from the Kelvin equation, relating the changes in the adsorbed or desorbed volume at different pressures to the pore radius, assuming cylindrical pore geometry. SEM-EDX measurements were performed using a JEOL JSM-5400 equipped with an INCAx X-ray detector. The measurements were carried out at energies between 5 to 20 kV.

The temperature-programmed experiments were conducted in a Micromeritics AutoChem 2920 equipped with a thermal conductivity detector and mass spectrometer. The temperature of the catalyst bed was measured with a K-type thermocouple touching the sample. Typically, 100 mg of the calcined samples (150–250 μm) were loaded into a quartz U-tube and pretreated under 60 Nml Ar min^{-1} at 500 °C for 1 h at atmospheric pressure. The temperature-programmed reduction (H_2-TPR) profile was recorded by heating the sample from 50 to 750 °C at a rate of 10 °C min^{-1}, while exposing it to a 5% H_2/Ar stream (60 Nml min^{-1}) and maintaining the temperature at 750 °C for 10 minutes. At the same time, a mass spectrometer measured the formed water during the process. The CO_2 adsorption capacity of the as-prepared samples was studied by CO_2 temperature-programmed desorption (CO_2-TPD). CO_2 adsorption was carried out under 60 Nml min^{-1} CO_2 at 50 °C for 2 hours. After evacuating the physically adsorbed CO_2 for 2 hours at 50 °C, the temperature-programmed desorption (TPD) profile was recorded by heating the sample from 50 to 500 °C at 10 °C min^{-1} under 60 Nml min^{-1} helium. The desorbed CO_2 was quantified by integrating the area under the deconvoluted desorption profile.

The surface chemical properties of samples were studied using X-ray photoelectron spectroscopy (XPS) with an SSI S-probe equipped with a monochromatic Al Kα source (hv = 1486.6 eV). Data acquisition was carried out under ultra-high vacuum conditions (9×10^{-7} Pa). Survey scans were measured at a constant pass energy of 140.8 eV. High-resolution scans were recorded at 90.15 eV for Zr 3d, Zn 2p, O 1s, and C 1s core level for ZrO_2, $Zn_{0.07}ZrO_y$-500, $Zn_{0.19}ZrO_y$-500, $Zn_{0.19}ZrO_y$-700, and $Zn_{0.19}ZrO_y$-800. All binding energies were calibrated using the C 1s peak of adventitious carbon at a binding energy of 284.8 eV.

Diffuse Reflectance Infrared Fourier Transform Spectroscopy (DRIFTS) measurements were conducted at 10 bar using a Harrick flow reactor equipped with ZnSe windows mounted in a Praying Mantis accessory within a Bruker Tensor 27 FTIR. To clarify the effect of Zn doping on ZrO_2, we selected ZrO_2, $Zn_{0.19}ZrO_y$, and $Zn_{0.56}ZrO_y$ for our DRIFT study. 30 mg of samples were diluted with 100 mg KBr and placed in the sample holder cup of a high-temperature cell. After pretreatment at 400 °C for 1 hour under an Ar atmosphere, background IR spectra were collected under Ar. The gas mixture was then introduced into the cell *via* mass flow controllers, and each spectrum was recorded at a resolution of 4 cm^{-1}, with an average of 32 scans per spectrum. In the CO_2 adsorption experiment, CO_2 was adsorbed by flowing 2 ml min^{-1} CO_2 in 16 ml min^{-1} Ar for 40 minutes, followed by the removal of weakly adsorbed species under Ar. For the methanol adsorption experiment, 2.3 ml min^{-1} of methanol with 130 ml min^{-1} Ar was introduced for 30 minutes at 200 °C. After methanol adsorption, physically adsorbed species were removed in an 130 ml min^{-1} Ar flow, and the spectra of the remaining adsorbed methanol were collected.

2.2.1. CO_2 hydrogenation. The performance of the catalysts in CO_2 hydrogenation was assessed at 45 bar and 300–400 °C in a high-pressure plug flow reactor with an internal diameter of 9 mm equipped with a 3 mm thermowell. Typically, 300 mg of the sieved catalyst (150–250 μm), diluted with 300 mg of quartz (150–250 μm), was loaded between two layers of quartz wool within the isothermal zone of the reactor. The catalysts underwent a one-hour pretreatment under 100 Nml min^{-1} Ar at 400 °C. They were then cooled to 300 °C, after which the reactant gas mixture was introduced through calibrated Bronckhorst mass flow controllers, maintaining a ratio of $H_2:CO_2:Ar$ = 3 : 1 : 1 at constant pressure and flowrate (45 bar and GHSV = 21 000 Nml g_{cat}^{-1} h^{-1}). The reaction temperature was incrementally increased from 300 to 400 °C in intervals of 25 °C and held for 2 hours at each temperature to establish steady-state conditions. The stability of the $Zn_{0.19}ZrO_y$-500 catalyst was evaluated by varying the reaction temperature and subsequently returning to the initial temperature, allowing for assessment of its performance consistency and resilience under elevated temperatures. The outlet gas line was maintained at 150 °C to prevent condensation of the reaction products. The reaction effluent was analysed online using a TRACE-1310 GC analyser equipped with Rt-Ubond (FID), Hayesep N and ShinCarbon-ST (1st TCD), and RT-QBond and RT-MolSieve 5A (2nd TCD) columns. The fulfilment of the Wheeler–Weisz and Carberry criteria confirmed the absence of transport limitations. The catalysts' performance was evaluated by calculating CO_2 conversion ($X(CO_2)$), methanol selectivity ($S(CH_3OH)$), and methanol space–time yield ($STY(CH_3OH)$) as follows:

$$X(CO_2) = \frac{F(CO_2)_{in} - F(CO_2)_{out}}{F(CO_2)_{in}} \times 100\% \quad (1)$$

$$S(CH_3OH) = \frac{F(CH_3OH)}{F(CO_2)_{in} - F(CO_2)_{out}} \times 100\% \quad (2)$$

$$STY(CH_3OH) = \frac{F(CH_3OH) \times MW(CH_3OH)}{V \times m_{catalyst}} \quad (3)$$

where F represents the volumetric flow rate calculated based on the Ar internal standard, $MW(CH_3OH)$ is the molecular weight of methanol, $m_{catalyst}$ is the catalyst weight in grams, and V is the molar volume of an ideal gas at normal conditions.

Open Access Article. Published on 12 December 2024. Downloaded on 2/17/2026 1:18:50 AM. This article is licensed under a Creative Commons Attribution 3.0 Unported Licence.

3. Results and analysis

3.1. Structure and general properties of the Zn_xZrO_y catalysts

The preparation of the Zn_xZrO_y precipitate follows a commonly used coprecipitation recipe comparable to other studies on CTM.[7,13] Seven different Zn/Zr molar ratios were used to prepare the ZrO_2, $Zn_{0.01}ZrO_y$, $Zn_{0.07}ZrO_y$, $Zn_{0.19}ZrO_y$, $Zn_{0.28}ZrO_y$, $Zn_{0.44}ZrO_y$ and $Zn_{0.56}ZrO_y$ precursors. After calcination at 500 °C, their physical properties and those of the ZnO sample as an extra reference were measured (Table 1). As reported in the literature, $Zn_{0.19}ZrO_y$ performs best in CTM conversion and selectivity at 350 °C.[7] This sample is, therefore, besides the standard 500 °C calcination temperature, also calcined at 550, 700, and 800 °C. Different levels of Zn addition and calcination temperatures are expected to change the main crystal phase of the bulk and distribute Zn differently between bulk and surface.[38] The bulk phase correlates to surface properties that underpin heterogeneous catalysis through exposed crystal planes and surface energy, including porosity, surface area, and texture.

Elemental analysis using scanning electron microscopy equipped with energy-dispersive X-ray spectroscopy (SEM-EDX) confirmed the successful Zn addition into ZrO_2 (Tables 1 and S1†). In XRD (Fig. 1), no ZnO crystals were detected in the samples with Zn/Zr ratios of 0.01–0.19, indicating that Zn is either finely distributed within these samples, present as small-sized crystallites (<3 nm), or is amorphous. On samples with Zn/Zr = 0.44–0.56, a hexagonal ZnO phase is visible beside the main ZrO_2 phase. Calcination of $Zn_{0.19}ZrO_y$ at 800 °C also causes ZnO phase separation and ZrO_2 phase transition to monoclinic and tetragonal.

The higher surface Zn/Zr ratio detected in XPS (Table 1), compared to the nominal elemental composition, suggests an enrichment of Zn near the surface,[12,23] implying the formation of an imperfect mixed metal oxide with a higher concentration of Zn in the skin layer than in the bulk; increasing the calcination temperature to 700 °C results in a higher concentration of Zn near the surface. Upon calcination at 800 °C, however, the Zn surface excess decreases (Fig. S2†), correlating with the appearance of ZnO crystals in XRD due to sintering.

Three main ZrO_2 phases are found in the XRD spectra: tetragonal, monoclinic, and cubic (Fig. 1a). In agreement with earlier reports, pristine ZrO_2 contains monoclinic and tetragonal phases.[7] A small addition of Zn (Zn/Zr = 0.01) results in a partial phase transformation from monoclinic to tetragonal, while larger amounts of Zn lead to the appearance of a cubic phase. From Zn/Zr = 0.07 upwards, the lattice also contracts with increasing Zn content, indicated by the shift of the diffraction peak near 30° to higher angles (Fig. 1b). This shift is consistent with the displacement of Zr (0.82 Å) by the smaller Zn cation (0.74 Å)[15] within the crystal lattice. A Zn/Zr molar ratio ≥ 0.07 leads to the formation of the cubic phase, as evidenced by the presence of symmetrical single peaks instead of double peaks at 2θ = 35.5°, 50.9° and 60.5°. ZnO remains undetectable up to Zn/Zr = 0.19. Excess Zn in the $Zn_{0.28}ZrO_y$-500 sample, surpassing the solid solution limit (Zn/Zr = 0.24),[23] alters the crystalline structure (Fig. 1b). The alteration induced by high zinc concentration broadens the peaks, shrinks the unit cell due to inhomogeneously strained crystallites, and shifts the diffraction peaks to higher angles.[7,39,40] The broadening peaks may indicate the presence of multiple phases within the material.[7] In $Zn_{0.44}ZrO_y$-500 and $Zn_{0.56}ZrO_y$-500, the excess ZnO gives rise to measurable diffractions, in addition to the cubic ZrO_2 diffractions.

Calcining the $Zn_{0.19}ZrO_y$ sample at higher temperatures (Fig. 1c) maintains the cubic phase at least up to 700 °C. At 800 °C, ZnO phase separation and cubic phase transformation to tetragonal and monoclinic phases occur.

Table 1 Properties of the as-synthesised samples

Sample	Crystal phase[a]	Surface area[b] ($m^2\ g^{-1}$)	Pore volume × 10^{-3}[c] ($cm^3\ g^{-1}$)	Avg. Pore size[c] (Å)	$n(H_2)$[d] (μmol g^{-1})	$n(CO_2)$[e] (μmol g^{-1})	Zn/Zr (molar ratio)			XPS (mol%)		
							Nominal composition	EDX[f]	XPS	Zr	O	Zn
ZnO	h-ZnO	31.5	230	316	—	1.6	—	—	—	—	—	—
ZrO_2	(m + t) ZrO_2	21.9	26	45	20.3	14.0	—	—	—	24.8	75.2	—
$Zn_{0.01}ZrO_y$-500	t-Phase	24.5	28	40	28.5	16.2	0.01	0.01	0.01	41.0	58.4	0.6
$Zn_{0.07}ZrO_y$-500	c-Phase	35.9	47	48	37.4	23.3	0.07	0.05	0.18	26.0	69.3	4.7
$Zn_{0.19}ZrO_y$-500	c-Phase	31.2	50	58	44.6	26.3	0.19	0.13	0.22	23.1	71.8	5.1
$Zn_{0.28}ZrO_y$-500	c-Phase	22.8	46	54	41.4	37.5	0.28	0.20	0.30	30.7	60.3	9.0
$Zn_{0.44}ZrO_y$-500	c-Phase +h-ZnO	17.5	32	66	72.5	5.3	0.44	0.48	0.59	28.1	55.2	16.7
$Zn_{0.56}ZrO_y$-500	c-Phase +h-ZnO	12.9	32	91	116.8	3.8	0.56	0.66	0.76	25.1	55.8	19.1
$Zn_{0.19}ZrO_y$-550	c-Phase	34.0	55	58	41.0	26.9	0.19	0.12	0.29	24.5	68.4	7.1
$Zn_{0.19}ZrO_y$-700	c-Phase	9.2	35	154	27.3	37.9	0.19	0.11	0.43	20.4	70.8	8.8
$Zn_{0.19}ZrO_y$-800	(m + t) phases +h-ZnO	1.1	9	322	23.3	2.6	0.19	0.10	0.24	23.0	71.6	5.5

[a] Identified in XRD (m: monoclinic, t: tetragonal, and c: cubic phase). [b] Determined using the BET method. [c] Determined from BJH adsorption isotherm. [d] Measured by integrating the peaks in H_2-TPR between 50–700 °C. [e] Measured by integrating the peaks in CO_2-TPD between 50–500 °C. [f] Calculated from EDX results at 20 kV electron beam energy.

 This journal is © The Royal Society of Chemistry 2025

Open Access Article. Published on 12 December 2024. Downloaded on 2/17/2026 1:18:50 AM.
This article is licensed under a Creative Commons Attribution 3.0 Unported Licence.

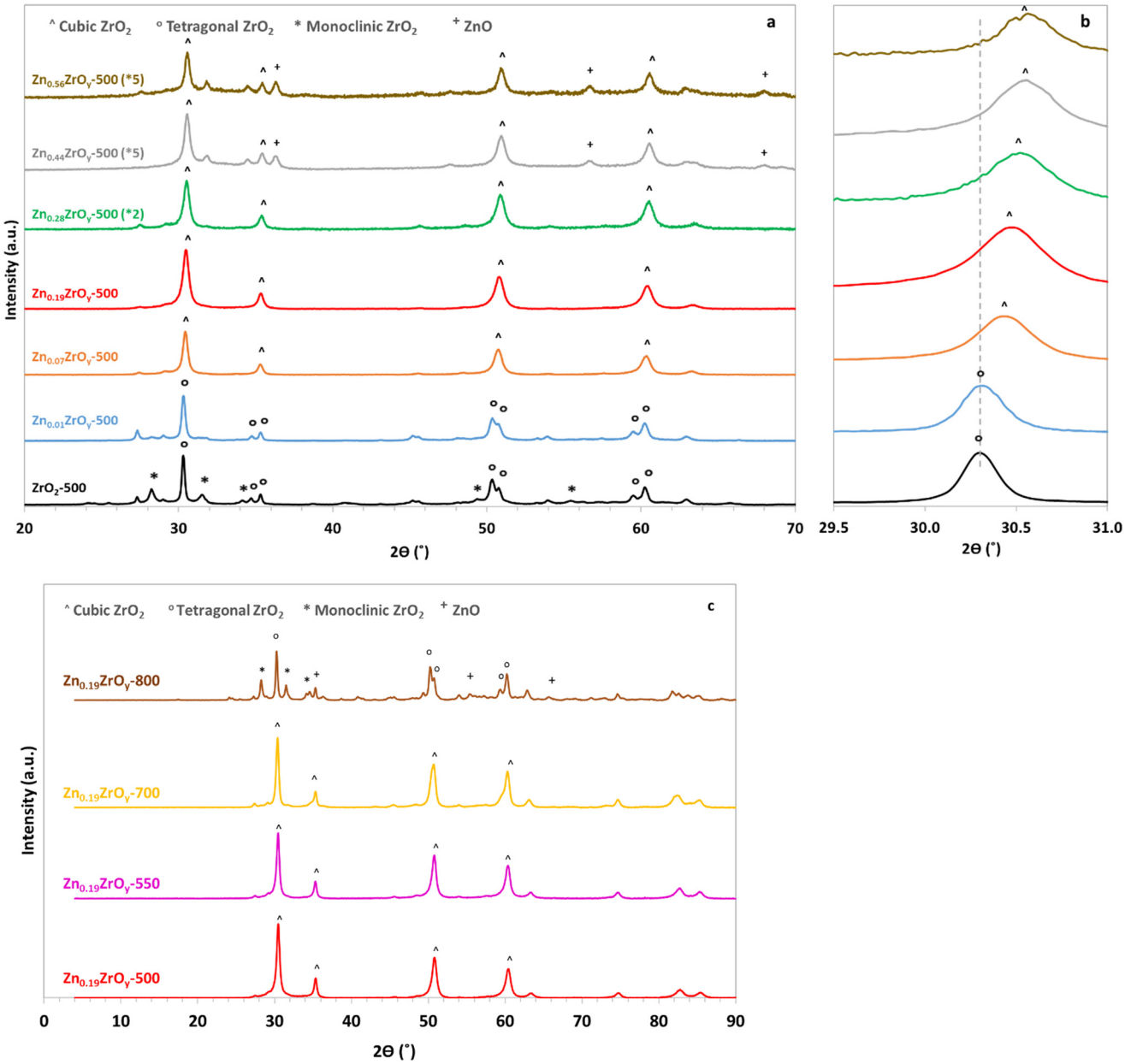

Fig. 1 (a) XRD patterns of Zn_xZrO_y-500 catalysts, (b) enlarged XRD patterns of Zn_xZrO_y-500 catalysts in the 2θ range of 29.5–31.0°, and (c) XRD patterns of $Zn_{0.19}ZrO_y$-*T* calcined at 500, 550, 700, and 800 °C (m-ZrO_2: PDF card 81.1314, t-ZrO_2: PDF card 50-1089, c-ZrO_2: PDF card 65-0461, and h-ZnO: PDF card 05-0664).

The samples' Raman spectra (Fig. 2 and ESI† section 2 – Raman spectroscopy) confirm the same crystal phases as those measured by XRD.

Table 1 and Fig. S1† present the nitrogen adsorption/desorption results, all indicating mesoporous materials. Up to Zn/Zr = 0.28, surface area and pore volume increase with Zn loading. Beyond this, surface area decreases. The $Zn_{0.44}$-ZrO_y-500 and $Zn_{0.56}ZrO_y$-500 isotherms resemble a bimodal mesoporous material, combining ZrO_2 and ZnO isotherms (Fig. S1a†). The region corresponding to $P/P^0 > 0.87$ implies the presence of larger mesopores attributed to the formation of ZnO particles, consistent with the XRD results. The other hysteresis region, within the range $0.45 < P/P^0 < 0.87$, represents the smaller mesopores of the mixed oxide. Elevating the calcination temperature to 700 °C and 800 °C alters the pore geometry, resulting in partially blocked pores (Fig. S1b†) and reduced surface area. The pore size distribution in Fig. S1c and d† illustrates changes in pore size resulting from zinc addition and the influence of calcination temperature on pore size distribution. The graphs show that pore enlargement occurs with calcination temperature exceeding 550 °C.

The Zr 3d and Zn 2p XPS spectra are shown in Fig. 3. The ZrO_2 profile can be fitted with three Gaussian-shaped doublets,

Open Access Article. Published on 12 December 2024. Downloaded on 2/17/2026 1:18:50 AM.
This article is licensed under a Creative Commons Attribution 3.0 Unported Licence.

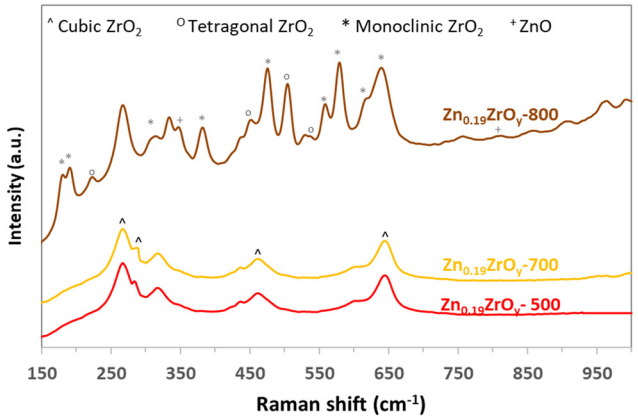

Fig. 2 Raman spectra of $Zn_{0.19}ZrO_y$-*T* calcined at 500, 700, and 800 °C.

each exhibiting a spin–orbital splitting of 2.4 eV, typical for zirconia. The bands centred at 180.9 and 182.3 eV are assigned to the monoclinic and tetragonal phases of ZrO_2, respectively.[41] The shift of the bands upon adding Zn indicates an alteration in the electronic and structural properties of Zr species in Zn_x-ZrO_y.[42] The high energy band centred at 182.6 eV corresponds to bulk Zr in cubic ZrO_2, indicating the phase transformation from tetragonal to cubic.[43,44] The low energy band at 181.3 eV is assigned to Zr in Zn–O–Zr motifs.[9,23,38,42,45,46] Zinc incorporation generates new surface Zr species in lower oxidation states, with a 179.9 eV centred XPS band, especially in the $Zn_{0.19}ZrO_y$-500 sample. Elevating the calcination temperature to 700 °C leads to a decrease in the concentration of Zr species in lower oxidation states, Fig. 3a and Table S2.†

Further increasing the calcination temperature to 800 °C shifts the Zr $3d_{5/2}$ bands to 180.9 and 182.3 eV, resembling the Zr 3d doublets observed in the pure ZrO_2 spectrum. This shift is attributed to the phase transformation of zirconia and the formation of monoclinic and tetragonal crystals at 800 °C, consistent with the XPS spectra observed for pure ZrO_2.

The Zn 2p spectra of the samples are shown in Fig. 3b. The binding energies of Zn $2p_{3/2}$ and Zn $2p_{1/2}$ in pure hexagonal ZnO centre at 1021.0 and 1044.1 eV, respectively.[42] Metallic Zn has a similar binding energy to ZnO, but isolated metallic Zn is not expected in these samples. The presence of Zn species at higher binding energy (1022.6 eV) in Zn_xZrO_y originates from the different coordination structures, suggesting that the Zn species are in contact with the oxygen of ZrO_2, forming Zn–O–Zr bonds.[46] This coordination environment, with higher electronegativity than the oxygen ligand in bulk ZnO, contributes to the observed shift in binding energy[38] and suggests a charge transfer between O^{2-}, Zr^{4+}, and Zn^{2+}.[45] These observations point to the possible incorporation of Zn into the ZrO_2 lattice, forming a mixed oxide. The Zn–O–Zr species disappear after calcination above

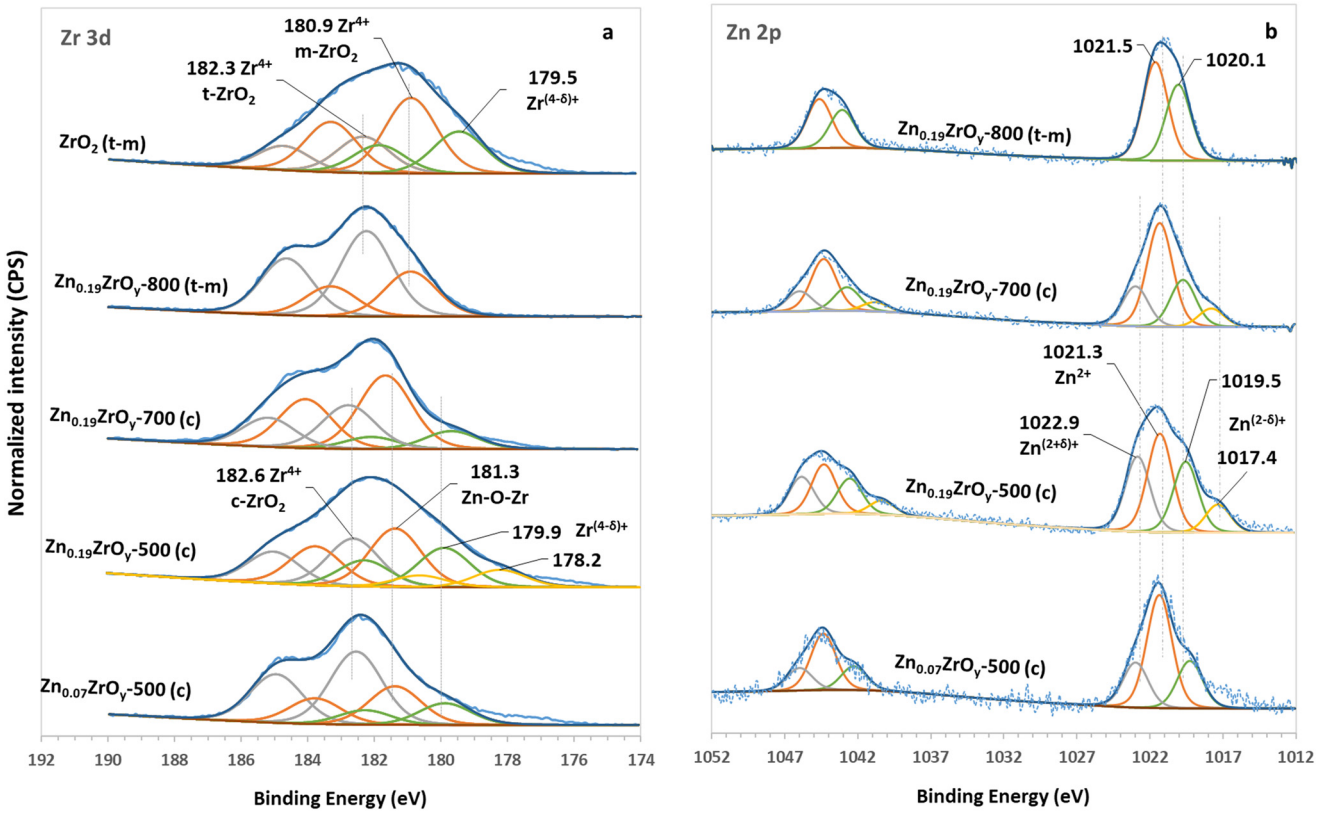

Fig. 3 XPS spectra of (a) Zr 3d in ZrO_2, $Zn_{0.07}ZrO_y$-500, $Zn_{0.19}ZrO_y$-500, $Zn_{0.19}ZrO_y$-700, and $Zn_{0.19}ZrO_y$-800 and (b) Zn 2p in $Zn_{0.07}ZrO_y$-500, $Zn_{0.19}ZrO_y$-500, $Zn_{0.19}ZrO_y$-700, and $Zn_{0.19}ZrO_y$-800.

 This journal is © The Royal Society of Chemistry 2025

Open Access Article. Published on 12 December 2024. Downloaded on 2/17/2026 1:18:50 AM.
This article is licensed under a Creative Commons Attribution 3.0 Unported Licence.

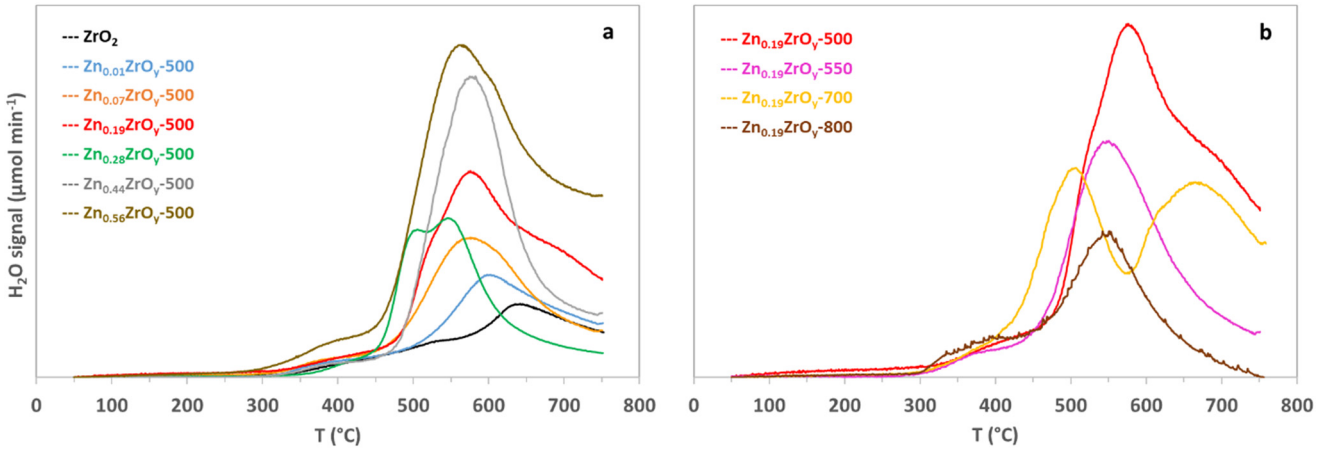

Fig. 4 Temperature-programmed H_2 reduction of (a) Zn_xZrO_y-500 catalysts and (b) $Zn_{0.19}ZrO_y$-*T* calcined at 500, 550, 700, and 800 °C.

700 °C due to the reduced contact between Zn and ZrO_2 related to the decreased surface area[38] and the formation of ZnO particles. Zn $2p_{3/2}$ and Zn $2p_{1/2}$ peaks become broader in $Zn_{0.19}ZrO_y$-500, originating from the partially charged Zn species. Increasing the calcination temperature to 700 °C reduces the 1017.4 eV band associated with $Zn^{(2-\delta)+}$ species, and this peak disappears entirely when the sample is calcined at 800 °C. The high-intensity peak centred at 1020.1 eV in $Zn_{0.19}ZrO_y$-800 is likely linked to the phase-separated ZnO species at the interface of ZrO_2.

The reducibility of the catalysts with H_2 is directly relevant to the activation of H_2 required for the CO_2 hydrogenation catalysis.[7] Fig. 4 shows H_2 temperature-programmed reduction profiles. The reduction of ZrO_2 is challenging and requires high temperatures.[13] Increasing the Zn/Zr ratio up to 0.19 progressively shifts the reduction to lower temperatures and increases the reducibility (quantified in Table 1), revealing the presence of more reducible oxygen species on the surface, which aligns with the observation of low binding energies in Zr and Zn XPS. In the $Zn_{0.44}ZrO_y$-500 and $Zn_{0.56}ZrO_y$-500 samples, the exposed ZnO particles result in noticeable H_2 consumption compared to the $Zn_{0.01}ZrO_y$-500 sample. The $Zn_{0.28}ZrO_y$-500 reduction profile shifts to lower temperatures, likely due to the formation of nano-sized ZnO particles with facilitated reduction compared to bulk ZnO. Increasing the calcination temperature gradually shifts the reduction to lower temperatures. In the $Zn_{0.19}ZrO_y$-700 sample, the low-temperature reduction can be attributed to the enrichment of the surface with Zn, as seen in XPS. In the $Zn_{0.19}ZrO_y$-800 sample, ZnO phase separation lowers the initial reduction temperatures.

CO_2 activation is generally linked to the acid–base properties of the zirconia catalyst surface, with basic surface OH sites forming bicarbonate and acid–base Lewis pairs forming monodentate and bidentate carbonate species.[47,48] The changes in ZrO_2 basicity upon Zn incorporation and the impact of calcination temperature were assessed using temperature-programmed CO_2 desorption (CO_2-TPD, Fig. 5). Deconvolution of the profiles (Fig. S4†) reveals three desorption features in each sample. According to their peak desorption temperatures, these correspond to weak (100 °C), medium (150–190 °C), and strong (>200 °C) basic sites. The medium and strong basic sites have been linked to chemisorbed CO_2 on Zn–O–Zr sites or surface oxygen vacancies.[8] CO_2 adsorption gradually increases with Zn loading from 14.0 μmol g^{-1} for ZrO_2 to 37.5 μmol g^{-1}

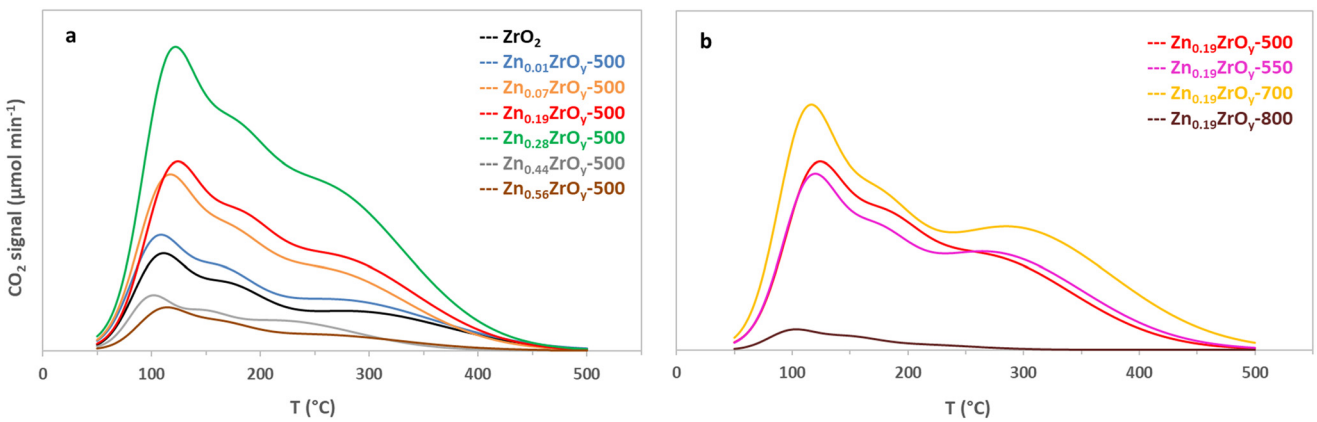

Fig. 5 Temperature-programmed CO_2 desorption of (a) Zn_xZrO_y-500 catalysts and (b) $Zn_{0.19}ZrO_y$-*T* calcined at 500, 550, 700, and 800 °C.

Open Access Article. Published on 12 December 2024. Downloaded on 2/17/2026 1:18:50 AM.
This article is licensed under a Creative Commons Attribution 3.0 Unported Licence.

for $Zn_{0.28}ZrO_y$-500, and then declines sharply (Table 1). Introducing zinc in a Zn/Zr ratio of 0.01 leads to a 17% increase in total CO_2 adsorption without notable alterations in the CO_2 desorption trend (Fig. 5a). This correlates with the transition of monoclinic zirconia to the tetragonal phase, characterized by higher basicity compared to the monoclinic phase,[49] and results in a marginal enhancement in catalyst activity. In the ZrO_2 catalyst comprising monoclinic and tetragonal phases, strong surface CO_2 adsorption sites are present. The addition of Zn, however, reduces the strength of these strong basic sites, likely due to the phase transformation from monoclinic, which contains stronger adsorption sites,[50] to tetragonal and cubic phases. Weaker basic sites are reported to facilitate CO_2 activation and its conversion to formate.[51] Increasing the Zn/Zr ratio up to 0.28 enhances the number of basic sites. The CO_2 desorption profiles of $Zn_{0.07}ZrO_y$-500 and $Zn_{0.19}ZrO_y$-500 exhibit remarkable similarity. The strong basic sites account for half of the total basicity, and the introduction of Zn shifts the temperature of the strong basic sites to lower temperatures (Table S3†). A higher calcination temperature shifts the strong basic sites to slightly higher temperatures (Fig. 5b). At 700 °C, the temperature at which the catalyst is on the verge of phase transformation, the basicity increases to 37.9 μmol g^{-1}. With a further increase in the calcination temperature to 800 °C, the basicity decreases sharply, primarily attributable to limited surface area (see Table 1) and the accumulation of ZnO crystals on the surface, which have low CO_2 adsorption capacity.

3.2. DRIFTS

Understanding the adsorption of CO_2 and methanol on ZrO_2 and Zn_xZrO_y mixed oxides is helpful to unravel the effect of Zn on surface interactions and catalytic behaviour. To this end, we studied the formation of surface species from CO_2 and methanol adsorption, followed by evacuation under argon.

3.2.1. CO_2 interaction with Zn_xZrO_y. On pure ZrO_2, CO_2 adsorption at 325 °C initially results in the formation of weakly interacting (wi-HCO_3^-) as well as monodentate bicarbonates (m-HCO_3^-), and carbonates (m-CO_3^{2-}). Over time, bidentate bicarbonates (b-HCO_3^-) and carbonates (b-CO_3^{2-}) also appear, with their intensities progressively increasing, Fig. 6a and S5.† The formation of bicarbonates (HCO_3^-) indicates the presence of surface OH^- groups,[52] while carbonates (CO_3^{2-}) derive from interaction with surface oxygens. After evacuation under Ar, the weakly interacting and monodentate bicarbonates disappear and the intensity of the monodentate carbonate decreases, indicating the removal of less stable surface species (Fig. 6b).

On $Zn_{0.19}ZrO_y$-500, CO_2 initially adsorbs as monodentate carbonates (m-CO_3^{2-}) species and weakly interacting bicarbonates (wi-HCO_3^-). With time, again bidentate carbonates (b-CO_3^{2-}) emerge, but now accompanied by the appearance of polydentate carbonates (p-CO_3^{2-}), Fig. 6a and S5.† Following evacuation under Ar (Fig. 6b), the weakly interacting bicarbonates (wi-HCO_3^-) disappear, the monodentate carbonates (m-CO_3^{2-}) decrease, the polydentate carbonates (p-CO_3^{2-}) remain stable, and the DRIFTS features of the bidentate carbonates shift to lower wavenumbers, indicating changes in their binding strength. The formation of bidentate carbonates at different wavelengths, 1578 cm^{-1} and 1564 cm^{-1}, is reported to correspond to two slightly different structural arrangements without further specification.[52]

The addition of Zn alters the surface sites, as observed in DRIFTS, and this coincides with changes in CO_2 adsorption behaviour, as observed in CO_2-TPD (Fig. 5). A commonly

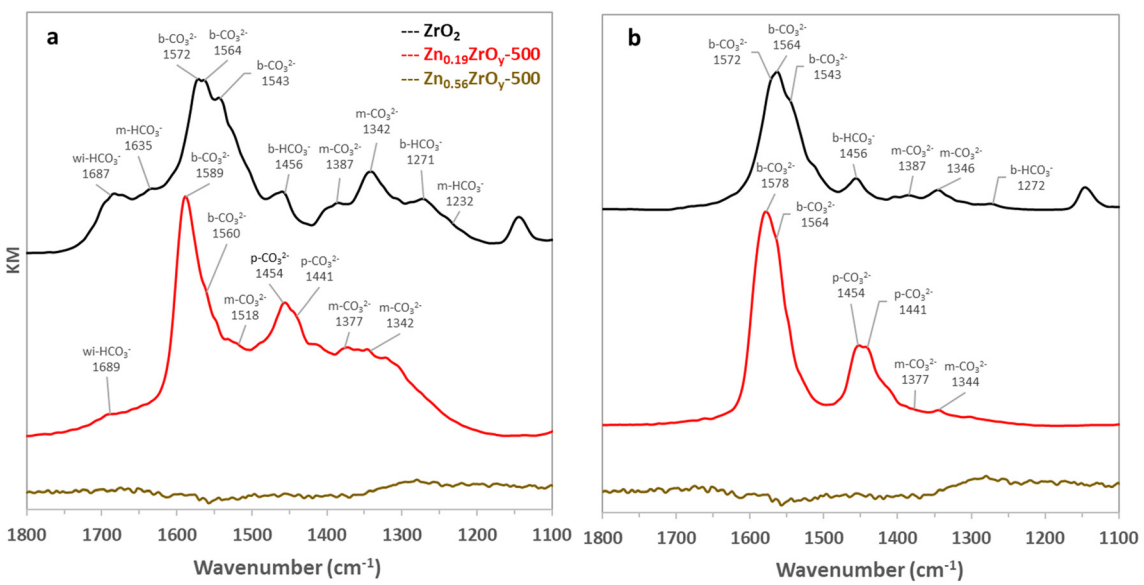

Fig. 6 DRIFT spectra of (a) CO_2 adsorption at 325 °C and 10 bar on ZrO_2, $Zn_{0.19}ZrO_y$-500, and $Zn_{0.56}ZrO_y$-500 after 40 minutes under 2 ml min^{-1} CO_2 and 16 ml min^{-1} Ar and (b) after 40 minutes evacuation at 325 °C and 10 bar under 16 ml min^{-1} Ar (m: monodentate, b: bidentate, wi: weakly interacting, and p: polydentate species).

 This journal is © The Royal Society of Chemistry 2025

Open Access Article. Published on 12 December 2024. Downloaded on 2/17/2026 1:18:50 AM. This article is licensed under a Creative Commons Attribution 3.0 Unported Licence.

stated explanation is an alteration of surface OH groups,[13,17,52,53] however the underlying drivers remain unclear. A possible explanation is an altered surface OH distribution on different ZrO_x phases. The monoclinic phase is described to be rich in surface OH groups,[17,52,54] while the cubic phase exposes facets with less surface OH.[55] XRD analysis (Fig. 1) indicates a shift towards the cubic phase upon Zn incorporation, but the correspondence to the amount of surface bicarbonates in DRIFTS and CO_2-TPD is not straightforward. Additionally, XPS data (Fig. 3) confirm the formation of Zn–O–Zr sites on the surface upon Zn addition. These Zn–O–Zr sites provide new adsorption sites,[13] possibly supporting the polydentate adsorption of carbonate, characterized by peaks at 1400–1480 cm^{-1}.[17,54]

Limited CO_2 adsorption on $Zn_{0.56}ZrO_y$-500 is in line with the formation of ZnO covering the surface, as confirmed by XRD and N_2 physisorption. This is consistent with the limited CO_2 adsorption capability of ZnO, as evidenced by the CO_2-TPD results (Fig. 5).

3.2.2. Methanol interaction with Zn_xZrO_y. Methanol adsorbs on metal oxides surfaces either associatively as intact methanol or dissociatively, forming a methoxy group and a proton. Associative adsorption of methanol *via* its oxygen atom occurs on sufficiently strong Lewis acid sites (LAS) that are not surrounded by highly basic sites. When the LAS is adjacent to basic sites and is not strong enough to favour associative adsorption, a Lewis acid–base pair (LAB) enables dissociative adsorption.[56–58] On ZrO_2, (Fig. 7) methanol exclusively adsorbs dissociatively, forming methoxy species through interactions with Lewis acid Zr^{4+} sites adjacent to lattice oxygen basic sites (LAB). In contrast, on $Zn_{0.19}ZrO_y$-500, additionally LAS-bound methanol is formed (bands at 1100, 2870, and 2960 cm^{-1}), suggesting the presence of new adsorption sites. This is likely achieved by an altered distribution of basic sites on the surface, facilitating the adsorption of intact methanol.

Dissociative methanol adsorption is observed on all tested samples, but on $Zn_{0.56}ZrO_y$-500, these peaks shift to higher wavenumbers, indicating further changes in the surface's electronic environment due to increased Zn content and ZnO formation. The peak intensity at 1160 cm^{-1} on ZrO_2 also decreases and shifts to 1150 cm^{-1} upon Zn addition, reflecting alterations in the adsorption sites.

3.3. Performance test

The performance for CO_2 hydrogenation was evaluated at 45 bar and 300–400 °C for all synthesized catalysts. Methanol and CO were the main products. Trace amounts of methane and dimethyl ether were also detected in the reactor effluent. Methane formation occurs only at elevated temperatures, above 350 °C, reaching a maximum formation of 0.25% of the methanol over $Zn_{0.56}ZrO_y$-500 at 400 °C. DME is produced through the sequential dehydration of methanol on acid sites, reaching a maximum formation of 3.11% of the methanol over $Zn_{0.07}ZrO_y$-500 at 375 °C. The CTM performance of $Zn_{0.19}ZrO_y$-500 at 350 °C was tested by increasing the reaction temperature and then returning to 350 °C. The catalyst maintained stable methanol selectivity and STY throughout temperature fluctuations, demonstrating its robustness and ability to perform well under changing thermal conditions (Fig. S6†).

Fig. 8a illustrates the temperature dependence of CO_2 conversion and methanol selectivity. Zinc introduction into

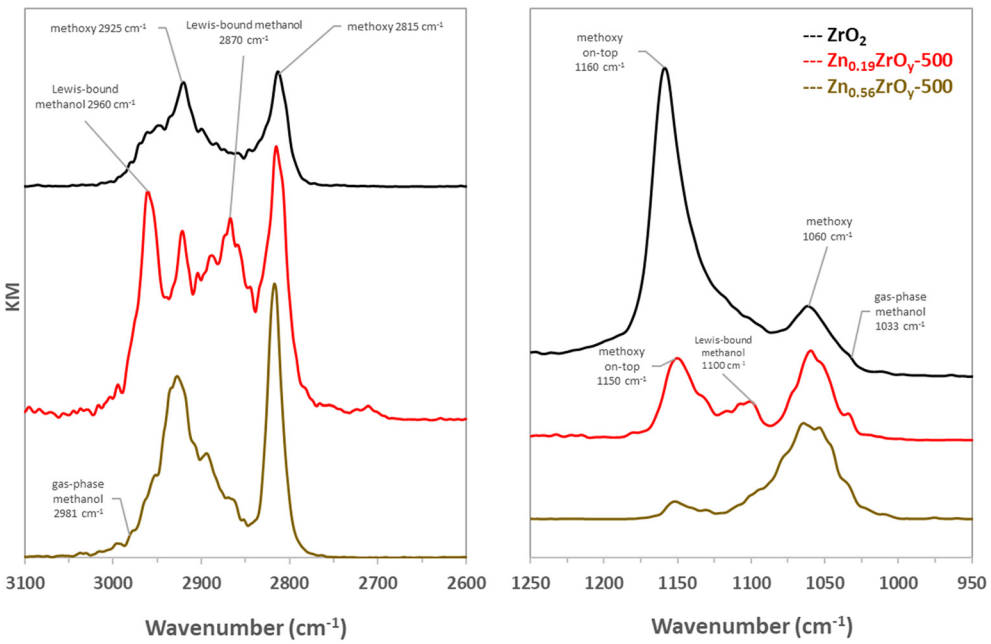

Fig. 7 DRIFT spectra of methanol adsorption at 200 °C and 10 bar on ZrO_2, $Zn_{0.19}ZrO_y$-500, and $Zn_{0.56}ZrO_y$-500 (the spectra were recorded after evacuation of physically adsorbed species under a flow of 130 ml min^{-1} Ar).

Open Access Article. Published on 12 December 2024. Downloaded on 2/17/2026 1:18:50 AM.
This article is licensed under a Creative Commons Attribution 3.0 Unported Licence.

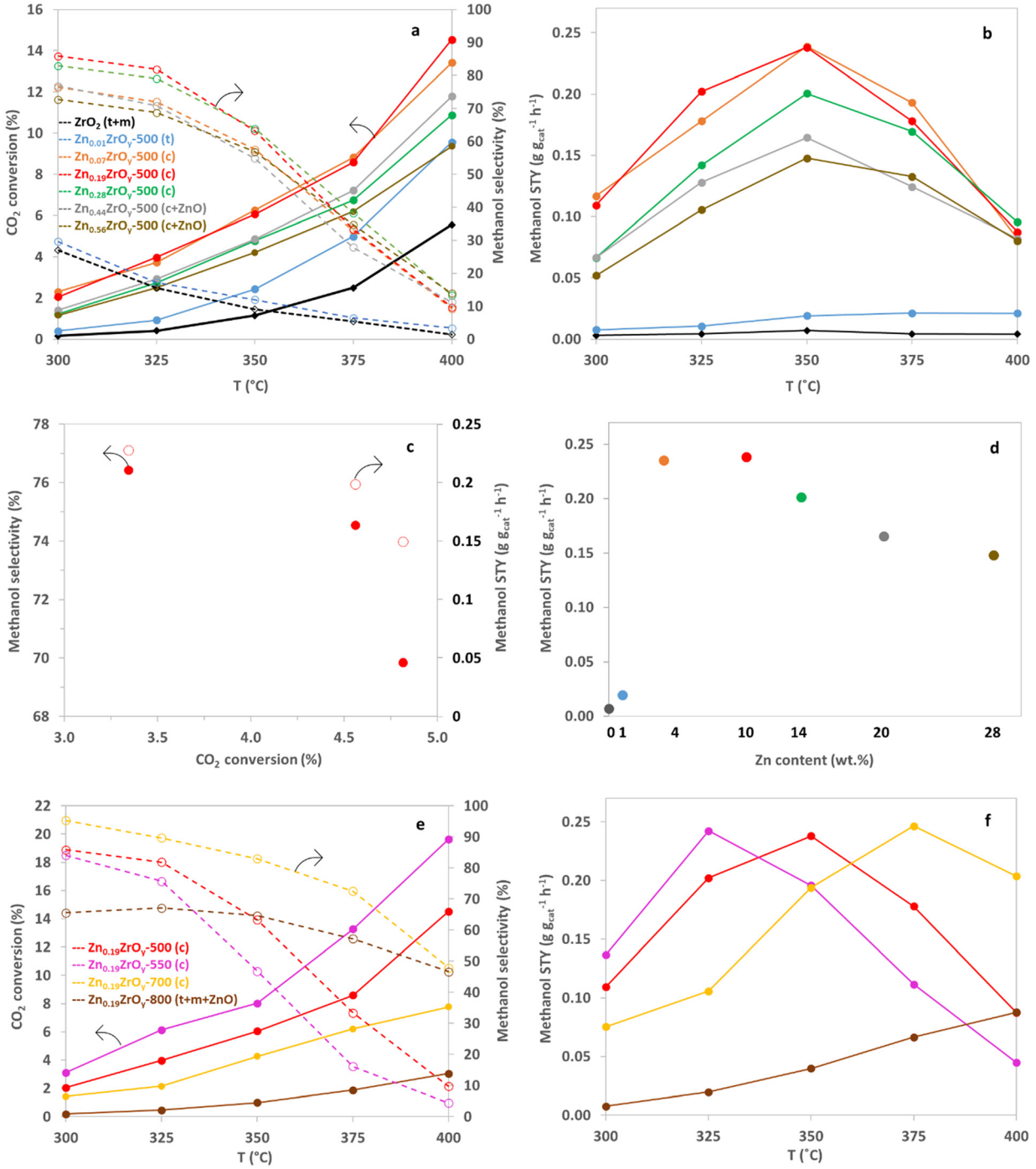

Fig. 8 Effect of temperature on (a) CO_2 conversion and methanol selectivity and (b) methanol STY of Zn_xZrO_y-500 catalysts, at 45 bar, $H_2:CO_2:Ar$ = 3 : 1 : 1, and GHSV = 21 000 Nml g_{cat}^{-1} h^{-1}. (c) Methanol selectivity *versus* CO_2 conversion on $Zn_{0.19}ZrO_y$-500 at 325 °C, 45 bar, $H_2:CO_2:Ar$ = 3 : 1 : 1, and GHSV = 31 500, 21 000, and 15 750 Nml g_{cat}^{-1} h^{-1}. (d) Effect of Zn loading on methanol STY at 350 °C, 45 bar, $H_2:CO_2:Ar$ = 3 : 1 : 1, and GHSV = 21 000 Nml g_{cat}^{-1} h^{-1}. (e) Effect of temperature on CO_2 conversion and methanol selectivity and (f) methanol STY of $Zn_{0.19}ZrO_y$-*T* catalysts, at 45 bar, $H_2:CO_2:Ar$ = 3 : 1 : 1, and GHSV = 21 000 Nml g_{cat}^{-1} h^{-1} (full lines: CO_2 conversion-dotted lines: methanol selectivity).

zirconia increases both CO_2 conversion and methanol selectivity across the temperature range. A Zn/Zr ratio of 0.01 has a negligible impact on the catalyst's CTM activity compared to pure ZrO_2. This doping level was also insufficient to stabilize the cubic phase. Samples containing Zn/Zr = 0.07–0.19 exhibit the highest CO_2 conversion among the tested samples. For reaction temperatures up to 350 °C, the selectivity to methanol maximally increases to more than threefold that of the Zn/Zr = 0.01 catalyst for the Zn/Zr = 0.19 catalyst, with the major increase with Zn doping occurring between Zn/Zr = 0.01 and 0.07. However, selectivity sharply declines above 350 °C, especially for the Zn/Zr ≥ 0.07

 This journal is © The Royal Society of Chemistry 2025

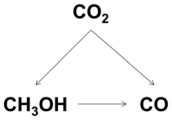

Scheme 1 CO_2 hydrogenation to methanol and CO and sequential reaction of methanol.

Open Access Article. Published on 12 December 2024. Downloaded on 2/17/2026 1:18:50 AM. This article is licensed under a Creative Commons Attribution 3.0 Unported Licence.

catalysts. The decline in selectivity with increasing conversion, induced by decreasing the flow rate (Fig. 8c), for $Zn_{0.19}ZrO_y$-500, suggests sequential reactions of methanol, Scheme 1.

For all catalysts with a Zn/Zr > 0.01, the methanol space–time yield (STY) peaks at 350 °C. The maximum methanol STY, 0.24 g g_{cat}^{-1} h^{-1}, is achieved with Zn/Zr = 0.07, for which a dominant cubic phase was found. This high STY is maintained up to Zn/Zr = 0.19, after which it gradually decreases with further increases in Zn/Zr ratios (Fig. 8b), accompanied by the formation of hexagonal ZnO. Although overall and surface Zn/Zr ratios vary, the catalytic activity is similar for $Zn_{0.07}ZrO_y$-500 and $Zn_{0.19}ZrO_y$-500 (Fig. 8d). The decrease in catalyst activity at higher Zn loadings up to Zn/Zr = 0.56 (in agreement with the literature),[7] suggests that the quantity of zinc does not necessarily lead to a rise in the number of active sites. Instead, it tends to augment the abundance of other sites, such as ZnO, with lower activity levels.

These results align with literature, where CO_2 hydrogenation at 320–350 °C, 20–50 bar, GHSV = 24 000 ml g_{cat}^{-1} h^{-1}, and H_2 : CO_2 = 3–4 gives a methanol selectivity ranging from 74 to 86%, with methanol formation rates of 0.2–0.3 g g_{cat}^{-1} h^{-1}.[13,22,33,34,59,60] An exception was observed for 13% ZnO–ZrO_2, which achieved a higher methanol formation rate of 0.5 g g_{cat}^{-1} h^{-1} under the same conditions.[7] Operating at lower GHSV values of 4000–10 800 ml g_{cat}^{-1} h^{-1} did not enhance performance, with the methanol formation rate dropping to 0.15–0.18 g g_{cat}^{-1} h^{-1}.[8,61] An overview of CTM catalysis in literature is included in the ESI† (Table S4, ESI† section 7).

We selected $Zn_{0.19}ZrO_y$-500 as the best-performing catalyst and conducted catalytic tests on samples calcined at 550, 700, and 800 °C (Fig. 8e). Within the examined temperature range, conversion is highest for $Zn_{0.19}ZrO_y$-550 but declines for higher calcination temperatures. Methanol selectivity becomes less temperature-dependent when using catalysts calcined at 700 and 800 °C. Fig. 8f illustrates the methanol space–time yield plotted against temperature. Higher calcination temperatures shift the point of maximum STY to a higher temperature.

4. Discussion

4.1. Preparation parameters for different zirconia phases

Through varying degrees of zinc doping and different calcination temperatures, we obtained Zn_xZrO_y materials of monoclinic, tetragonal, and cubic polymorphs, as demonstrated in earlier literature.[62] Monoclinic zirconia is stable at low temperatures, transitioning to the tetragonal phase at around 1170 °C, and then into the cubic phase at 2370–2680 °C.[63] The stability of the tetragonal or cubic phase depends on grain size and chemical composition. Particles larger than 30 nm are most stable as monoclinic ZrO_2, those smaller than 14 nm as tetragonal ZrO_2, and particles smaller than 6 nm as the metastable cubic ZrO_2 phase.[43,64–66] The tetragonal or cubic zirconia can additionally be stabilized by doping an aliovalent cation such as Zn^{2+} into zirconia,[16,67–69] by adding stabilizing oxides,[70] or by adjusting the calcination temperature.[63] Doped cations replace some zirconium ions in the crystal lattice, altering its electronic structure and introducing lattice strains that hinder oxygen atoms' movement and inhibit phase transitions from cubic to other crystalline phases.[43,71–73] With increasing Zn doping, the dominant ZrO_2 crystal phase alters from monoclinic to tetragonal and then to cubic. At calcination temperatures above 800 °C, the kinetic barriers preserving the metastable cubic phase are surpassed,[74,75] leading to the transition of the material into tetragonal and monoclinic phases.

In this study, beyond Zn/Zr = 0.28, ZnO phase separation happens, observed as hexagonal ZnO. Synthesizing catalysts with a Zn/Zr ratio up to 0.28 increased surface area, pore volume, and basicity. However, the Zn/Zr ratio exceeding 0.44 resulted in bimodal mesoporous materials, indicating the formation of ZnO particles and lower surface area, leading to inferior catalytic performance.

4.2. Surface property correlations and CTM catalysis

Adding zinc at a Zn/Zr ratio of 0.01 has a negligible impact on the catalyst's activity in methanol synthesis and is insufficient to stabilize the cubic phase. With Zn/Zr = 0.07 and 0.19, enhanced methanol STY, 34 times higher than the unpromoted ZrO_2 catalyst, is observed at 350 °C and this coincides with the phase transition to cubic phase. With Zn/Zr ratios of 0.44–0.56, again lower activity is obtained (Fig. S8†) which coincides with zinc phase separation forming hexagonal ZnO. This aligns with existing literature,[23] indicating other types of Zn sites, such as ZnO, with lower activity levels are formed at such high Zn/Zr ratios.

This study aims to assess the structure–function relationship by which the Zn_xZrO_y crystal phase influences CTM catalysis. The investigated samples yield a large variety of surface physical and chemical properties. From the correlation plot in Fig. 9a, it is clear that many variables correlate strongly among the assessed samples. When focusing exclusively on the pure cubic-phase samples, however, the correlations are very different, highlighting distinct behaviour within this subset. Moreover, the correlation plot indicates a strong positive correlation between cubic phase and selectivity, space–time yield, and CO_2 conversion in CTM at 350 °C. The other phases on the other hand show a negative correlation. The addition of Zn to ZrO_2 enables and enhances CO_2 conversion and methanol selectivity, as shown in Fig. 9b. Most interestingly, while a general trade-off between conversion and selectivity is observed among the tested samples, those with a pure cubic phase achieve the highest

Open Access Article. Published on 12 December 2024. Downloaded on 2/17/2026 1:18:50 AM.
This article is licensed under a Creative Commons Attribution 3.0 Unported Licence.

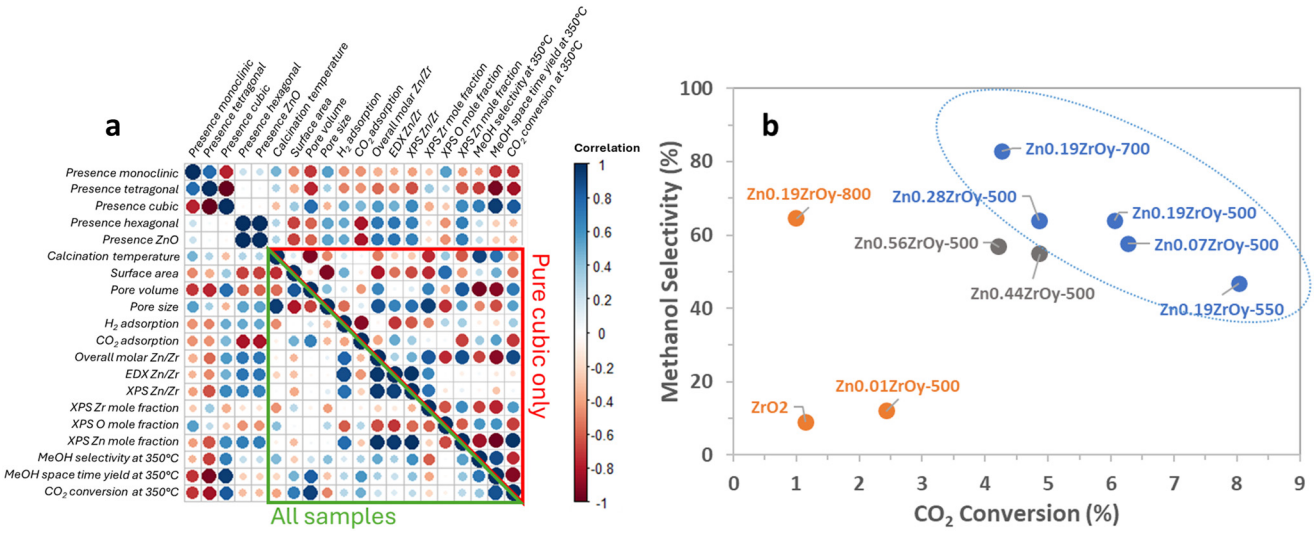

Fig. 9 (a) Surface property correlations and CTM catalysis within all samples and (b) methanol selectivity *versus* CO_2 conversion at 350 °C, 45 bar, $H_2:CO_2:Ar = 3:1:1$, and GHSV = 21 000 Nml g_{cat}^{-1} h^{-1} (blue colour: pure cubic-phase, grey colour: cubic-phase + h-ZnO, and orange colour: the rest of the samples).

selectivity for methanol at a given conversion at 350 °C. Although ZrO_2 and $Zn_{0.19}ZrO_y$-800 convert CO_2 to a similar extent and exhibit comparable crystal phases, the presence of Zn in $Zn_{0.19}ZrO_y$-800 promotes selective methanol production in the reaction.

The cubic materials are also those with the highest pore volume and surface area, smallest pore size, and highest surface Zn. We therefore additionally look at surface properties in relation to pore volume, surface area, or surface zinc concentration as these metrics more suitably pinpoint desirable properties of the surface structure on a molecular level. Individual two-dimensional plots are shown in Fig. 10 and 11, and ESI† section 9 – parameters correlation where it can also be seen that samples with a pure cubic phase occupy distinct regions in the plots (shown in blue).

For all samples, there is a clear positive correlation between specific surface area and conversion and for samples containing cubic phase, there is a clear negative correlation between selectivity and pore volume (Fig. S7†) in which the cubic-phase-free samples do not fit. From Fig. 9b and S8b,† while conversion correlates strongly positively with pore volume (and thus negatively with selectivity, as is logically expected) for all samples, the pure cubic samples still demonstrate high selectivity at high pore volumes. This may, in part, be attributed to their unique combining of high CO_2 adsorption per pore volume and selectivity as well as their low H_2 uptake per pore volume (Fig. 10). From the available data, we cannot draw full conclusions on what sets the cubic phase samples apart from the others in this regard, but the observed beneficial effect of lower H_2 uptake is surprising. It counterintuitively seems to favour selectivity to the more reduced methanol over CO, potentially by limiting further methanol decomposition to CO, while hydrogen activation and spillover are commonly seen as the rate-determining step (RDS) in methanol synthesis.[74,75] The

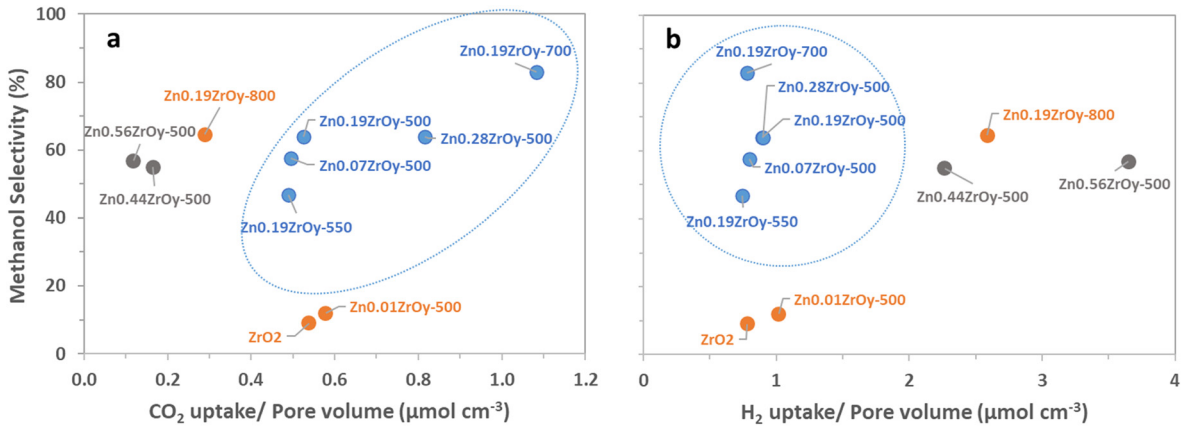

Fig. 10 Effect of pore-volume normalized (a) CO_2 uptake and (b) H_2 uptake on methanol selectivity at 350 °C, 45 bar, $H_2:CO_2:Ar = 3:1:1$, and GHSV = 21 000 Nml g_{cat}^{-1} h^{-1} (blue colour: pure cubic-phase, grey colour: cubic-phase + h-ZnO, and orange colour: the rest of the samples).

 This journal is © The Royal Society of Chemistry 2025

Open Access Article. Published on 12 December 2024. Downloaded on 2/17/2026 1:18:50 AM.
This article is licensed under a Creative Commons Attribution 3.0 Unported Licence.

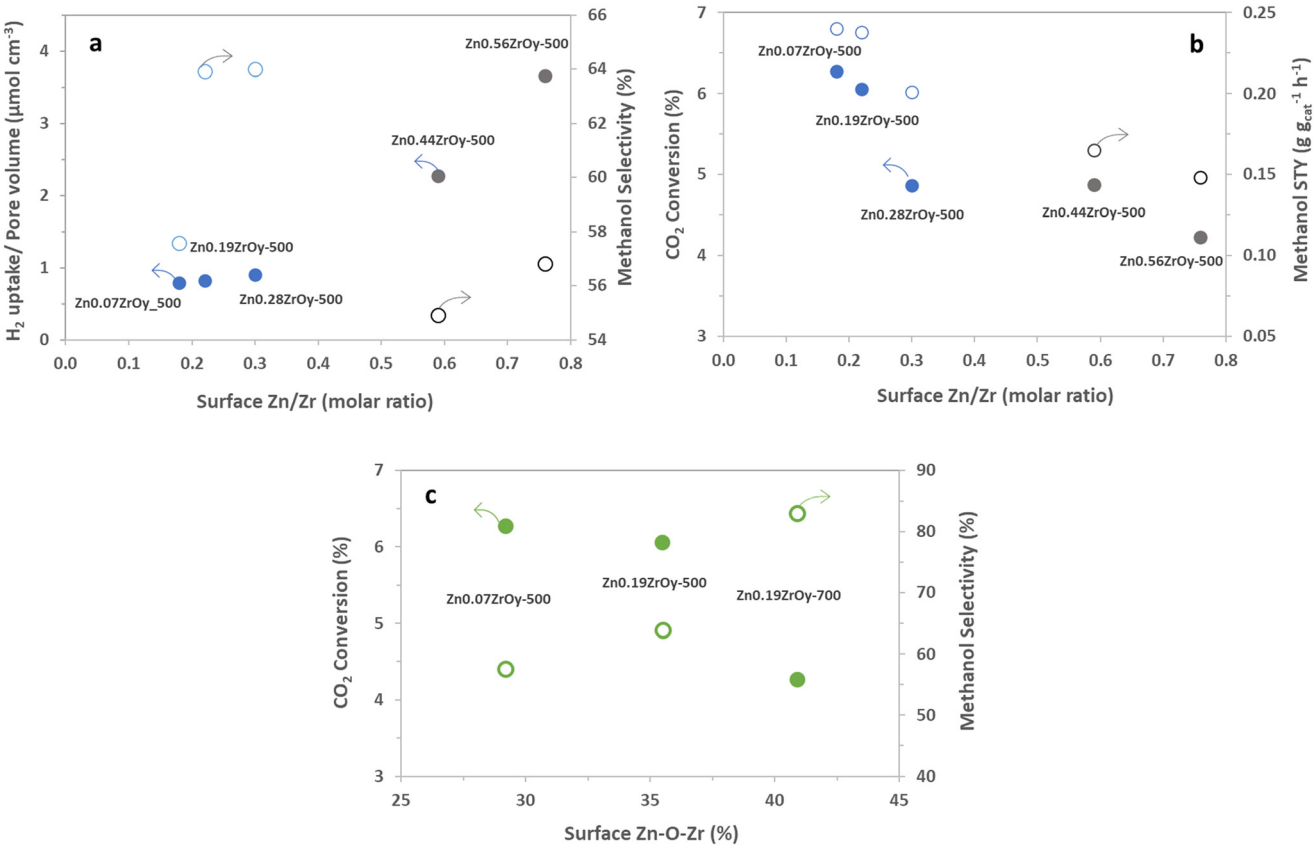

Fig. 11 For a sub-selection of the measured samples, all with a dominant cubic phase; effect of (XPS) surface Zn/Zr ratio on (a) pore volume normalized H_2 uptake (solid points) and methanol selectivity (empty points), and (b) CO_2 conversion (solid points) and methanol STY (empty points), (blue colour: pure cubic-phase and grey colour: cubic-phase + h-ZnO) and (c) effect of (XPS) surface Zn–O–Zr species on CO_2 conversion (solid points) and methanol selectivity (empty points), at 350 °C, 45 bar, $H_2:CO_2:Ar$ = 3 : 1 : 1, and GHSV = 21 000 Nml g_{cat}^{-1} h^{-1}.

existence of the cubic phase may confound solid-phase diffusion during synthesis, which could enhance favourable zinc speciation at the surface. While surface zinc is essential, CTM catalysis appears to be more advantageous with cubic phase catalysts for reasons not fully addressed by current data. Coupled with literature, linking CO_2 adsorption to oxygen vacancy sites[17,21,22] suggests that surface zinc indeed facilitates CO_2 adsorption. However, the cubic phase seems to provide a specific combination of oxygen vacancies and surface zinc, promoting CO formation only to a limited extent compared to other catalysts.[15]

The role of the crystal phase in methanol synthesis was highlighted in a recent study examining monoclinic *versus* tetragonal phases. The tetragonal phase achieved significantly higher methanol selectivity (81% *versus* 39%) and STY (0.04 *versus* 0.02 g g_{cat}^{-1} h^{-1}) compared to the monoclinic phase at 320 °C, using a Zn_xZrO_y catalyst.[26] In the present study, methanol STY reached 0.20 g g_{cat}^{-1} h^{-1} on the cubic phase sample, with comparable selectivity, underscoring the importance of stabilizing the optimal crystal phase. Clearly, certain crystal phases, in particular the cubic one, enhance the performance of Zn_xZrO_y catalyst in CTM. In addition to the Zn-induced phase change observed in XRD (Fig. 1), DRIFTS indicates that Zn influences surface basicity, which also affects CTM catalysis by means of CO_2 and methanol chemisorption (Fig. 5–7). Hence, Zn contributes to CTM catalysis by inducing structural changes in two ways. Disentangling the latter requires further study of the quantitative structure–function relations.

It is informative to further analyse surface Zn's electronic properties for the samples containing cubic phase Zn_xZrO_y, and their association with CTM catalysis (Fig. 11). For the cubic samples calcined at 500 °C, particularly in the ZnO phase-separated samples ($Zn_{0.44}ZrO_y$ and $Zn_{0.56}ZrO_y$), a positive correlation is observed between the increased surface Zn/Zr concentration and the pore-volume normalized H_2 uptake (Fig. 11a). This suggests a role for surface Zn (or ZnO) in steering selectivity through the surface density of adsorbed H_2. In Fig. 11a, methanol selectivity peaks at a surface Zn/Zr ratio of 0.2–0.4. However, further increasing the surface Zn/Zr ratio and the formation of ZnO particles negatively affects methanol selectivity. Fig. 11b confirms that CO_2 conversion and methanol STY are optimal within a narrow range of surface Zn/Zr ratios. More specifically, the presence of Zr–O–Zn bonds correlates positively with methanol selectivity and negatively with CO_2 conversion, (Fig. 11c), suggesting that H_2 activation over Zn–O–Zr sites is not rate controlling, since a higher Zn–O–Zr surface fraction yields a lower conversion. This implies that the electronic properties of the surface

Open Access Article. Published on 12 December 2024. Downloaded on 2/17/2026 1:18:50 AM. This article is licensed under a Creative Commons Attribution 3.0 Unported Licence.

atoms are crucial in determining the catalyst's behaviour, especially when the crystal phase is cubic. This electronic interaction is presumably more important than the physical characteristics of the pores, as it directly affects the reactivity and selectivity of the catalysts. This is supported by efforts to increase surface area using the evaporation-induced self-assembly method (EISA) to achieve 96 m^2 g^{-1} compared to 48 m^2 g^{-1} with the coprecipitation method, which resulted in only a minor increase in CO_2 conversion, from 4% to 5.5% at 320 °C.[33]

5. Conclusions

This study explored the influence of Zn on the structure of Zn_xZrO_y and its catalytic performance in CO_2 hydrogenation to methanol. Zinc incorporation into the zirconia lattice induces a phase transformation from monoclinic and tetragonal to mainly tetragonal phase in $Zn_{0.01}ZrO_y$-500. The cubic phase becomes dominant from a Zn/Zr ratio of 0.07. Catalysts with a Zn/Zr ratio of 0.07 and 0.19 demonstrate enhanced methanol formation. The cubic phase remains stable up to the calcination temperature of 700 °C, above which a transition to tetragonal and monoclinic phases occurs. The decreased catalytic activity of such samples can be attributed to the formation of agglomerated ZnO particles and the phase transformation.

An optimal zinc content for CTM catalysis facilitates the formation of a mixed oxide, resulting in the formation of the cubic phase and enhances CO_2 adsorption sites. Elevating the calcination temperature further indicates the significance of the cubic zirconia crystal phase. Within the pure cubic-phase samples, the surface Zn/Zr ratio and the concentration of Zr–O–Zn species correlate positively with CO_2 adsorption capacity and methanol selectivity. Insufficient zinc content fails to stabilize the cubic phase, while excessive zinc content leads to ZnO phase separation. Both are detrimental to catalyst performance. Although the surface Zn/Zr ratio shows a positive correlation with pore volume-normalized H_2 uptake, increased H_2 uptake does not necessarily translate to improved CTM performance. Rather, a narrow range of surface Zn/Zr is advantageous, enhancing both methanol selectivity and CO_2 conversion.

Further analysis of the catalysts at 350 °C reveals the underlying drivers for CO_2 conversion to methanol, indicating that moderate Zn doping combined with a pure cubic phase induces the most effective CTM catalysts regarding methanol space–time yield (STY). Because a variety of catalytically relevant surface properties vary simultaneously, pinpointing the exact reason for this observation on an active site level remains challenging, both from our collected data and existing literature. A possible explanation lies in the changed concentration and distribution of surface basicity on the zirconia surface. Nevertheless, we identify informative correlations for CTM catalysis and can conclude that a 'one-fits-all' explanation of the role of zinc in promoting ZrO_x catalysts for CTM is inadequate. It is an example of the commonly encountered complexity in catalytic structure–function relationships.

Data availability

The processed data supporting this article (N_2 physisorption, XPS, SEM-EDX, CO_2-TPD, DRIFTS and catalyst stability test) have been included as part of the ESI.† Raw data are available on request from the corresponding author.

Conflicts of interest

There are no conflicts to declare.

Acknowledgements

This project was financially supported by C^2O (Light-assisted and thermal heterogeneous catalysis for the direct conversion of CO_2 to olefins) Flanders Industry Innovation Moonshot (AIO SBO 2021 000 701).

References

1 G. Pacchioni, From CO_2 to Methanol on $Cu/ZnO/Al_2O_3$ Industrial Catalyst. What Do We Know about the Active Phase and the Reaction Mechanism?, *ACS Catal.*, 2024, **14**, 2730–2745.
2 S. Chen, J. Wang, Z. Feng, Y. Jiang, H. Hu, Y. Qu, S. Tang, Z. Li, J. Liu, J. Wang and C. Li, Hydrogenation of CO_2 to Light Olefins over $ZnZrO_x$/SSZ-13, *Angew. Chem., Int. Ed.*, 2024, **63**, 1–7.
3 Z. Li, J. Wang, Y. Qu, H. Liu, C. Tang, S. Miao, Z. Feng, H. An and C. Li, Highly Selective Conversion of Carbon Dioxide to Lower Olefins, *ACS Catal.*, 2017, **7**, 8544–8548.
4 M. Flores-Granobles and M. Saeys, Quantitative analysis of CO_2 emissions reduction potential of alternative light olefins production processes, *Green Chem.*, 2023, **25**, 6459–6471.
5 W. Zhang, S. Wang, S. Guo, Z. Qin, M. Dong, J. Wang and W. Fan, Effective conversion of CO_2 into light olefins along with generation of low amounts of CO, *J. Catal.*, 2022, **413**, 923–933.
6 P. Zhang, L. Ma, F. Meng, L. Wang, R. Zhang, G. Yang and Z. Li, Boosting CO_2 hydrogenation performance for light olefin synthesis over $GaZrO_x$ combined with SAPO-34, *Appl. Catal., B*, 2022, **305**, 121042.
7 J. Wang, G. Li, Z. Li, C. Tang, Z. Feng, H. An, H. Liu, T. Liu and C. Li, A highly selective and stable ZnO-ZrO_2 solid solution catalyst for CO_2 hydrogenation to methanol, *Sci. Adv.*, 2017, **3**, 1701290.
8 W. Zhang, S. Wang, S. Guo, Z. Qin, M. Dong, J. Wang and W. Fan, Effective conversion of CO_2 into light olefins over a bifunctional catalyst consisting of La-modified $ZnZrO_x$ oxide and acidic zeolite, *Catal. Sci. Technol.*, 2022, **12**, 2566–2577.
9 W.-H. Feng, M.-M. Yu, L.-J. Wang, Y.-T. Miao, M. Shakouri, J. Ran, Y. Hu, Z. Li, R. Huang, Y.-L. Lu, D. Gao and J.-F. Wu, Insights into Bimetallic Oxide Synergy during Carbon Dioxide Hydrogenation to Methanol and Dimethyl Ether

 This journal is © The Royal Society of Chemistry 2025

Open Access Article. Published on 12 December 2024. Downloaded on 2/17/2026 1:18:50 AM. This article is licensed under a Creative Commons Attribution 3.0 Unported Licence.

over $GaZrO_x$ Oxide Catalysts, *ACS Catal.*, 2021, **11**, 4704–4711.

10 L. Zhang, B. Geng, P. Wang, H. Kang, H. Xiao, J. Jia and H. Wu, Highly efficient $ZnCeZrO_x$/SAPO-34 catalyst for the direct conversion of CO_2 into light olefins under mild reaction conditions, *Appl. Catal., A*, 2023, **657**, 119141.

11 D. Salusso, E. Borfecchia and S. Bordiga, Combining X-ray Diffraction and X-ray Absorption Spectroscopy to Unveil Zn Local Environment in Zn-Doped ZrO_2 Catalysts, *J. Phys. Chem. C*, 2021, **125**, 22249–22261.

12 L. D. R. Silva-Calpa, P. C. Zonetti, C. P. Rodrigues, O. C. Alves, L. G. Appel and R. R. de Avillez, The $Zn_xZr_{1-x}O_{2-y}$ solid solution on m-ZrO_2: Creating O vacancies and improving the m-ZrO_2 redox properties, *J. Mol. Catal. A: Chem.*, 2016, **425**, 166–173.

13 Z. Feng, C. Tang, P. Zhang, K. Li, G. Li, J. Wang, Z. Feng and C. Li, Asymmetric Sites on the $ZnZrO_x$ Catalyst for Promoting Formate Formation and Transformation in CO_2 Hydrogenation, *J. Am. Chem. Soc.*, 2023, **145**, 12663–12672.

14 K. Lee, M. P. Dickieson, M. Jung, Y. Yang and N. Yan, Structure Sensitivity of $ZnZrO_x$ Catalysts in CO_2 Hydrogenation to Methanol: Significance of Surface Oxygen Content and Synthesis Strategy, *ACS Catal.*, 2024, **14**, 3074–3089.

15 L. H. Chagas, P. C. Zonetti, C. R. V. Matheus, C. R. K. Rabello, O. C. Alves and L. G. Appel, The Role of the Oxygen Vacancies in the Synthesis of 1, 3-Butadiene from Ethanol, *ChemCatChem*, 2019, **11**, 5625–5632.

16 E.-M. Köck, M. Kogler, T. Bielz, B. Klötzer and S. Penner, *In Situ* FT-IR Spectroscopic Study of CO_2 and CO Adsorption on Y_2O_3, ZrO_2, and Yttria-Stabilized ZrO_2, *J. Phys. Chem. C*, 2013, **117**, 17666–17673.

17 K. Pokrovski, K. T. Jung and A. T. Bell, Investigation of CO and CO_2 Adsorption on Tetragonal and Monoclinic Zirconia, *Langmuir*, 2001, **17**, 4297–4303.

18 T. J. Keskitalo, M. K. Veringa Niemelä and A. O. I. Krause, Modeling of the Adsorption and Desorption of CO_2 on Cu/ZrO_2 and ZrO_2 Catalysts, *Langmuir*, 2007, **23**, 7612–7619.

19 J. Kondo, H. Abe, Y. Sakata, K.-I. Maruya, K. Domen and T. Onishi, Infrared studies of adsorbed species of H_2, CO and CO_2 over ZrO_2, *J. Chem. Soc., Faraday Trans. 1*, 1988, **84**, 511–519.

20 F. Sha, S. Tang, C. Tang, Z. Feng, J. Wang and C. Li, The role of surface hydroxyls on $ZnZrO_x$ solid solution catalyst in CO_2 hydrogenation to methanol, *Chin. J. Catal.*, 2023, **45**, 162–173.

21 M. D. Rhodes and A. T. Bell, The effects of zirconia morphology on methanol synthesis from CO and H_2 over Cu/ZrO_2 catalysts Part I. Steady-state studies, *J. Catal.*, 2005, **233**, 198–209.

22 P. Ticali, D. Salusso, R. Ahmad, C. Ahoba-Sam, A. Ramirez, G. Shterk, K. A. Lomachenko, E. Borfecchia, S. Morandi, L. Cavallo, J. Gascon, S. Bordiga and U. Olsbye, CO_2 hydrogenation to methanol and hydrocarbons over bifunctional Zn-doped ZrO_2/zeolite catalysts, *Catal. Sci. Technol.*, 2021, **11**, 1249–1268.

23 S. Tada, N. Ochiai, H. Kinoshita, M. Yoshida, N. Shimada, T. Joutsuka, M. Nishijima, T. Honma, N. Yamauchi, Y. Kobayashi and K. Iyoki, Active Sites on $ZnZrO_x$ Solid Solution Catalysts for CO_2-to-Methanol Hydrogenation, *ACS Catal.*, 2022, **12**, 7748–7759.

24 Y. Kim, T. S. B. Trung, S. Yang, S. Kim and H. Lee, Mechanism of the Surface Hydrogen Induced Conversion of CO_2 to Methanol at Cu(111) Step Sites, *ACS Catal.*, 2016, **6**, 1037–1044.

25 E. A. Redekop, T. Cordero-Lanzac, D. Salusso, A. Pokle, S. Oien-Odegaard, M. F. Sunding, S. Diplas, C. Negri, E. Borfecchia, S. Bordiga and U. Olsbye, Zn Redistribution and Volatility in $ZnZrO_x$ Catalysts for CO_2 Hydrogenation, *Chem. Mater.*, 2023, **35**, 10434–10445.

26 X. Zhang, X. Yu, R. G. Mendes, P. Matvija, A. E. M. Melcherts, C. Sun, X. Ye, B. M. Weckhuysen and M. Monai, Highly Dispersed ZnO Sites in a ZnO/ZrO_2 Catalyst Promote Carbon Dioxide-to-Methanol Conversion, *Angew. Chem., Int. Ed.*, 2024, 202416899.

27 X. Zhang, G. Zhang, X. Zhou, Z. Wang, Y. Liu, J. Zhu, C. Song and X. Guo, Identification of the Active Sites on ZnO/ZrO_2 for CO_2 Hydrogenation to CO and Methanol, *Ind. Eng. Chem. Res.*, 2023, **62**, 21173–21181.

28 K. Tanabe and T. Yamaguchi, Acid-base bifunctional catalysis by ZrO_2 and its mixed oxides, *Catal. Today*, 1994, **20**, 185–197.

29 K. Tanabe, Surface and catalytic properties of ZrO_2, *Mater. Chem. Phys.*, 1985, **13**, 347–364.

30 N. R. Jaegers, V. Danghyan, J. Shangguan, C. Lizandara-Oueyo, P. Deshlahra and E. Iglesia, Heterolytic C–H Activation Routes in Catalytic Dehydrogenation of Light Alkanes on Lewis Acid–Base Pairs at ZrO_2 Surfaces, *J. Am. Chem. Soc.*, 2024, **146**, 25710–25726.

31 S. Kim, C. A. Jhaveri and E. Sasmaz, Impact of Yttria-Stabilized Zirconia on Direct CO_2 Hydrogenation to Light Olefins over a Tandem Catalyst Composed of In_2O_3/YSZ and SAPO-34, *Energy Fuels*, 2023, **37**, 7361–7371.

32 S. G. Giniyatova, A. L. Kozlovskiy, R. I. Shakirzyanov, N. O. Volodina, D. I. Shlimas and D. B. Borgekov, Structural, Dielectric, and Mechanical Properties of High-Content Cubic Zirconia Ceramics Obtained *via* Solid-State Synthesis, *Appl. Sci.*, 2023, **13**, 10989.

33 Z. Han, C. Tang, F. Sha, S. Tang, J. Wang and C. Li, CO_2 hydrogenation to methanol on ZnO-ZrO_2 solid solution catalysts with ordered mesoporous structure, *J. Catal.*, 2021, **396**, 242–250.

34 K. Lee, U. Anjum, T. P. Araújo, C. Mondelli, Q. He, S. Furukawa, J. Pérez-Ramírez, S. M. Kozlov and N. Yan, Atomic Pd-promoted $ZnZrO_x$ solid solution catalyst for CO_2 hydrogenation to methanol, *Appl. Catal., B*, 2022, **304**, 120994.

35 M. T. Nikolajsen, J.-C. Grivel, A. Gaur, L. P. Hansen, L. Baumgarten, N. C. Schjødt, U. V. Mentzel, J.-D. Grunwaldt, J. Sehested, J. M. Christensen and M. Høj, Surface ZnO_x on zirconia is highly active for high temperature methanol synthesis, *J. Catal.*, 2024, **431**, 115389.

Open Access Article. Published on 12 December 2024. Downloaded on 2/17/2026 1:18:50 AM. This article is licensed under a Creative Commons Attribution 3.0 Unported Licence.

36 F. C. F. Marcos, F. M. Cavalcanti, D. D. Petrolini, L. Lin, L. E. Betancourt, S. D. Senanayake, J. A. Rodriguez, J. M. Assaf, R. Giudici and E. M. Assaf, Effect of operating parameters on H_2/CO_2 conversion to methanol over Cu-Zn oxide supported on ZrO_2 polymorph catalysts: Characterization and kinetics, *Chem. Eng. J.*, 2022, **427**, 130947.

37 T. Witoon, J. Chalorngtham, P. Dumrongbunditkul, M. Chareonpanich and J. Limtrakul, CO_2 hydrogenation to methanol over Cu/ZrO_2 catalysts: Effects of zirconia phases, *Chem. Eng. J.*, 2016, **293**, 327–336.

38 C. Temvuttirojn, Y. Poo-Arporn, N. Chanlek, C. K. Cheng, C. C. Chong, J. Limtrakul and T. Witoon, Role of Calcination Temperatures of ZrO_2 Support on Methanol Synthesis from CO_2 Hydrogenation at High Reaction Temperatures over ZnO_x/ZrO_2 Catalysts, *Ind. Eng. Chem. Res.*, 2020, **59**, 5525–5535.

39 T. Yamamoto and A. Kurimoto, Ga Ion-doped ZrO_2 Catalyst Characterized by XRD, XAFS, and 2-Butanol Decomposition, *Anal. Sci.*, 2020, **36**, 41–46.

40 K. Anandan, K. Rajesh, K. Gayathri, S. Vinoth Sharma, S. G. Mohammed Hussain and V. Rajendran, Effects of rare earth, transition and post transition metal ions on structural and optical properties and photocatalytic activities of zirconia (ZrO_2) nanoparticles synthesized *via* the facile precipitation process, *Phys. E*, 2020, **124**, 114342.

41 P. Lackner, Z. Zou, S. Mayr, U. Diebold and M. Schmid, Using photoelectron spectroscopy to observe oxygen spillover to zirconia, *Phys. Chem. Chem. Phys.*, 2019, **21**, 17613–17620.

42 S. Han, D. Zhao, T. Otroshchenko, H. Lund, U. Bentrup, V. A. Kondratenko, N. Rockstroh, S. Bartling, D. E. Doronkin, J.-D. Grunwaldt, U. Rodemerck, D. Linke, M. Gao, G. Jiang and E. V. Kondratenko, Elucidating the Nature of Active Sites and Fundamentals for their Creation in Zn-Containing ZrO_2–Based Catalysts for Nonoxidative Propane Dehydrogenation, *ACS Catal.*, 2020, **10**, 8933–8949.

43 Y. Maithani, J. A. Khan, B. R. Mehta and J. P. Singh, Cubic phase optimization and influence of post-annealing on microstructure, optical, wetting, and nanomechanical properties of zirconia thin films, *Ceram. Int.*, 2023, **49**, 1048–1060.

44 K. Samson, M. Śliwa, R. P. Socha, K. Góra-Marek, D. Mucha, D. Rutkowska-Zbik, J. F. Paul, M. Ruggiero-Mikołajczyk, R. Grabowski and J. Słoczyński, Influence of ZrO_2 Structure and Copper Electronic State on Activity of Cu/ZrO_2 Catalysts in Methanol Synthesis from CO_2, *ACS Catal.*, 2014, **4**, 3730–3741.

45 J. Ding, Z. Li, W. Xiong, Y. Zhang, A. Ye and W. Huang, Structural evolution and catalytic performance in CO_2 hydrogenation reaction of $ZnO\text{-}ZrO_2$ composite oxides, *Appl. Surf. Sci.*, 2022, **587**, 152884.

46 Z. Zhang, Y. Huang, H. Ma, W. Qian, H. Zhang and W. Ying, Syngas-to-olefins over MOF-derived $ZnZrO_x$ and SAPO-34 bifunctional catalysts, *Catal. Commun.*, 2021, **152**, 106292.

47 D. Wierzbicki, R. Baran, R. Dębek, M. Motak, M. E. Gálvez, T. Grzybek, P. Da Costa and P. Glatzel, Examination of the influence of La promotion on Ni state in hydrotalcite-derived catalysts under CO_2 methanation reaction conditions: Operando X-ray absorption and emission spectroscopy investigation, *Appl. Catal., B*, 2018, **232**, 409–419.

48 L. J. I. Coleman, W. Epling, R. R. Hudgins and E. Croiset, Ni/Mg-Al mixed oxide catalyst for the steam reforming of ethanol, *Appl. Catal., A*, 2009, **363**, 52–63.

49 Z.-Y. Ma, C. Yang, W. Wei, W.-H. Li and Y.-H. Sun, Surface properties and CO adsorption on zirconia polymorphs, *J. Mol. Catal. A: Chem.*, 2005, **227**, 119–124.

50 K. Taek Jung, Y. G. Shul and A. T. Bell, The Preparation and Surface Characterization of Zirconia Polymorphs, *Korean J. Chem. Eng.*, 2001, **18**, 992–999.

51 Z. Zhang, L. Zhang, M. J. Hülsey and N. Yan, Zirconia phase effect in Pd/ZrO_2 catalyzed CO_2 hydrogenation into formate, *Mol. Catal.*, 2019, **475**, 110461.

52 B. Bachiller-Baeza, I. Rodriguez-Ramos and A. Guerrero-Ruiz, Interaction of Carbon Dioxide with the Surface of Zirconia Polymorphs, *Langmuir*, 1998, **14**, 3556–3564.

53 N. H. M. D. Dostagir, C. R. Tomuschat, K. Oshiro, M. Gao, J. Hasegawa, A. Fukuoka and A. Shrotri, Mitigating the Poisoning Effect of Formate during CO_2 Hydrogenation to Methanol over Co-Containing Dual-Atom Oxide Catalysts, *JACS Au*, 2024, **4**(3), 1048–1058.

54 F. C. F. Marcos, J. M. Assaf, R. Giudici and E. M. Assaf, Surface interaction of CO_2/H_2 mixture on mesoporous ZrO_2: Effect of crystalline polymorph phases, Appl, *Surf. Sci.*, 2019, **496**, 143671.

55 S. N. Basahel, T. T. Ali, M. Mokhtar and K. Narasimharao, Influence of crystal structure of nanosized ZrO_2 on photocatalytic degradation of methyl orange, *Nanoscale Res. Lett.*, 2015, **10**, 73.

56 L. E. Briand, W. E. Farneth and I. E. Wachs, Quantitative determination of the number of active surface sites and the turnover frequencies for methanol oxidation over metal oxide catalysts I. Fundamentals of the methanol chemisorption technique and application to monolayer supported molybdenum oxide catalysts, *Catal. Today*, 2000, **62**, 219–229.

57 L. J. Burcham, L. E. Briand and I. E. Wachs, Quantification of Active Sites for the Determination of Methanol Oxidation Turn-over Frequencies Using Methanol Chemisorption and *in Situ* Infrared Techniques. 2. Bulk Metal Oxide Catalysts, *Langmuir*, 2001, **17**, 6175–6184.

58 M. Badlani and I. E. Wachs, Methanol: A "Smart" Chemical Probe Molecule, *Catal. Lett.*, 2001, **75**, 137–149.

59 T. P. Araújo, J. Morales-Vidal, T. Zou, M. Agrachev, S. P. O. Willi, R. N. Grass, G. Jeschke, S. Mitchell, N. López and J. Pérez-Ramírez, Design of Flame-Made $ZnZrO_x$ Catalysts for Sustainable Methanol Synthesis from CO_2, *Adv. Energy Mater.*, 2023, **13**, 2204122.

60 Q. Ren, K. Yang, F. Liu, M. Yao, J. Ma, S. Geng and J. Cao, Role of the structure and morphology of zirconia in ZnO/ZrO_2 catalyst for CO_2 hydrogenation to methanol, *Mol. Catal.*, 2023, **547**, 113280–113280.

 This journal is © The Royal Society of Chemistry 2025

Open Access Article. Published on 12 December 2024. Downloaded on 2/17/2026 1:18:50 AM.
This article is licensed under a Creative Commons Attribution 3.0 Unported Licence.

61 D. Xu, X. Hong and G. Liu, Highly dispersed metal doping to ZnZr oxide catalyst for CO_2 hydrogenation to methanol: Insight into hydrogen spillover, *J. Catal.*, 2021, **393**, 207–214.
62 S. Tsunekawa, S. Ito, Y. Kawazoe and J.-T. Wang, Critical Size of the Phase Transition from Cubic to Tetragonal in Pure Zirconia Nanoparticles, *Nano Lett.*, 2003, **3**, 871–875.
63 T. Chraska, A. H. King and C. C. Berndt, On the size-dependent phase transformation in nanoparticulate zirconia, *Mater. Sci. Eng., A*, 2000, **286**, 169–178.
64 Y. L. Zhang, X. J. Jin, Y. H. Rong, T. Y. Hsu, D. Y. Jiang and J. L. Shi, The size dependence of structural stability in nano-sized ZrO_2 particles, *Mater. Sci. Eng., A*, 2006, **438–440**, 399–402.
65 S. Jayakumar, P. V. Ananthapadmanabhan, T. K. Thiyagarajan, K. Perumal, S. C. Mishra, G. Suresh, L. T. Su and A. I. Y. Tok, Nanosize stabilization of cubic and tetragonal phases in reactive plasma synthesized zirconia powders, *Mater. Chem. Phys.*, 2013, **140**, 176–182.
66 A. Bumajdad, A. Abdel Nazeer, F. Al Sagheer, S. Nahar and M. I. Zaki, Controlled Synthesis of ZrO_2 Nanoparticles with Tailored Size, Morphology and Crystal Phases *via* Organic/Inorganic Hybrid Films, *Sci. Rep.*, 2018, **8**, 22088.
67 S. Shukla and S. Seal, Mechanisms of room temperature metastable tetragonal phase stabilisation in zirconia, *Int. Mater. Rev.*, 2005, **50**, 45–64.
68 L. M. G. Rojas, C. A. Huerta-Aguilar, E. Navarrete, E. Llobet and P. Thangarasu, Enhancement of the CO_2 Sensing/Capture through High Cationic Charge in M-ZrO_2 (Li^+, Mg^{2+}, or Co^{3+}): Experimental and Theoretical Studies, *ACS Appl. Mater. Interfaces*, 2023, **15**, 25952–25965.
69 A. O. Zhigachev, V. V. Rodaev, D. V. Zhigacheva, N. V. Lyskov and M. A. Shchukina, Doping of scandia-stabilized zirconia electrolytes for intermediate-temperature solid oxide fuel cell: A review, *Ceram. Int.*, 2021, **47**, 32490–32504.
70 A. K. Nikumbh and P. V. Adhyapak, Formation characterization and rheological properties of zirconia and ceria-stabilized zirconia, *Nat. Sci.*, 2010, **2**, 694–706.
71 C. Colbea, D. Avram, B. Cojocaru, R. Negrea, C. Ghica, V. G. Kessler, G. A. Seisenbaeva, V. Parvulescu and C. Tiseanu, Full Tetragonal Phase Stabilization in ZrO_2 Nanoparticles Using Wet Impregnation: Interplay of Host Structure, Dopant Concentration and Sensitivity of Characterization Technique, *Nanomaterials*, 2018, **8**, 988–988.
72 M. Raza, D. Cornil, S. Lucas, R. Snyders, S. Konstantinidis and J. Cornil, Oxygen vacancy stabilized zirconia (OVSZ); a joint experimental and theoretical study, *Scr. Mater.*, 2016, **124**, 26–29.
73 W. Kim, M. Choi and K. Yong, Generation of oxygen vacancies in ZnO nanorods/films and their effects on gas sensing properties, *Sens. Actuators, B*, 2015, **209**, 989–996.
74 K. Bocam, C. Anunmana and T. Eiampongpaiboon, Grain size, crystalline phase and fracture toughness of the monolithic zirconia, *J. Adv. Prosthodont.*, 2022, **14**, 285–293.
75 N. C. Horti, M. D. Kamatagi, S. K. Nataraj, M. N. Wari and S. R. Inamdar, Structural and optical properties of zirconium oxide (ZrO_2) nanoparticles: effect of calcination temperature, *Nano Express*, 2020, **1**, 01002.